AGU PUBLICATIONS

JGR

Journal of Geophysical Research: Atmospheres

RESEARCH ARTICLE
10.1002/2013JD020831

Key Points:
- Ozone columns from European sensors reprocessed with an improved algorithm
- Soft-calibration of the reflectances improves the inter-sensor consistency
- High-quality data sets in excellent agreement with the SBUV v8.6 record

Correspondence to:
C. Lerot,
christophe.lerot@aeronomie.be

Citation:
Lerot, C., et al. (2014), Homogenized total ozone data records from the European sensors GOME/ERS-2, SCIAMACHY/Envisat, and GOME-2/MetOp-A, *J. Geophys. Res. Atmos.*, *119*, 1639–1662, doi:10.1002/2013JD020831.

Received 3 SEP 2013
Accepted 17 NOV 2013
Accepted article online 21 NOV 2013
Published online 12 FEB 2014

Homogenized total ozone data records from the European sensors GOME/ERS-2, SCIAMACHY/Envisat, and GOME-2/MetOp-A

C. Lerot[1], M. Van Roozendael[1], R. Spurr[2], D. Loyola[3], M. Coldewey-Egbers[3], S. Kochenova[1], J. van Gent[1], M. Koukouli[4], D. Balis[4], J.-C. Lambert[1], J. Granville[1], and C. Zehner[5]

[1]Belgian Institute for Space Aeronomy, Brussels, Belgium, [2]RT Solutions, Inc., Cambridge, Massachusetts, USA, [3]German Aerospace Center (DLR), Oberpfaffenhofen, Germany, [4]Laboratory of Atmospheric Physics, Aristotle University of Thessaloniki (AUTH), Thessaloniki, Greece, [5]ESA/ESRIN, Frascati, Italy

Abstract Within the European Space Agency's Climate Change Initiative, total ozone column records from GOME (Global Ozone Monitoring Experiment), SCIAMACHY (SCanning Imaging Absorption SpectroMeter for Atmospheric CartograpHY), and GOME-2 have been reprocessed with GODFIT version 3 (GOME-type Direct FITting). This algorithm is based on the direct fitting of reflectances simulated in the Huggins bands to the observations. We report on new developments in the algorithm from the version implemented in the operational GOME Data Processor v5. The a priori ozone profile database TOMSv8 is now combined with a recently compiled OMI/MLS tropospheric ozone climatology to improve the representativeness of a priori information. The Ring procedure that corrects simulated radiances for the rotational Raman inelastic scattering signature has been improved using a revised semi-empirical expression. Correction factors are also applied to the simulated spectra to account for atmospheric polarization. In addition, the computational performance has been significantly enhanced through the implementation of new radiative transfer tools based on principal component analysis of the optical properties. Furthermore, a soft-calibration scheme for measured reflectances and based on selected Brewer measurements has been developed in order to reduce the impact of level-1 errors. This soft-calibration corrects not only for possible biases in backscattered reflectances, but also for artificial spectral features interfering with the ozone signature. Intersensor comparisons and ground-based validation indicate that these ozone data sets are of unprecedented quality, with stability better than 1% per decade, a precision of 1.7%, and systematic uncertainties less than 3.6% over a wide range of atmospheric states.

1. Introduction

As a consequence of the 1987 Montreal Protocol and its subsequent amendments, most of the ozone-depleting substance emissions have been phased out, and one expects the stratospheric ozone layer to recover over the next few decades (e.g., *Bekki et al.*, 2011). However, significant uncertainty remains as to the timing of a return to pre-1980 ozone concentrations; this lack of certainty is mainly due to interactions with ongoing climate change and the continuing rise of greenhouse gas (GHG) emissions. For example, most climate-coupled models predict ozone recovery at northern midlatitudes to be much faster than that at southern midlatitudes, because of the stratospheric GHG-induced cooling [*Eyring et al.*, 2007; *Fleming et al.*, 2011]. For the same reason, a so-called "super-recovery" could be predicted for the Arctic region. On the other hand, climate change is expected to lead to an acceleration of the Brewer-Dobson circulation, which could prevent ozone from returning to its 1980 level in tropical regions [*Austin et al.*, 2010]. Since ozone is an important GHG, recovery of the ozone layer will have an impact on the global atmospheric radiative budget. Although additional atmospheric warming is expected, the range of the projected ozone radiative forcing values provided by current models is very large [*Bekki et al.*, 2013].

To address these questions and provide the most reliable projections, climate-coupled models require the assimilation of reliable and homogeneous long time series of accurate satellite ozone observations. The European Space Agency (ESA) has set up the Climate Change Initiative (CCI) program, which aims to realize the full potential of the long-term Earth Observation data records for a number of Essential Climate Variables (ECV); this includes the total ozone data record, on which we focus in this work. In particular, multisensor

satellite data products covering a large time period need to be generated in order to meet the requirements of the climate modeling community. Regarding the total ozone ECV, the target requirements defined within the Global Climate Observation System (GCOS) are a total uncertainty of 2% and a stability better than 1% per decade [*GCOS*, 2011]. Within the Ozone_cci project, a multisensor total ozone data record covering the period 1996–2012 has been constructed; this is based on observations from three European instruments, namely the Global Ozone Monitoring Experiment (GOME) aboard ERS-2, the SCanning Imaging Absorption SpectroMeter for Atmospheric CartograpHY (SCIAMACHY) on Envisat, and GOME-2 on MetOp-A.

These three UV–Visible spectrometer instruments are all mounted on sun-synchronous low Earth orbit (LEO) polar platforms with local equator crossing times of 10h30, 10h00, and 9h30, for ERS-2, Envisat, and MetOp-A, respectively. ESA's GOME is a nadir-viewing instrument with a spatial resolution of 320×40 km^2 [*Burrows et al*., 1999]. GOME provided high quality measurements between 1995 and 2011 with global coverage achieved in 3 days for the first 8 years of the mission until June 2003, when coverage was significantly reduced due to the failure of the satellite tape storage system. SCIAMACHY [*Bovensmann et al*., 1999], a German/Dutch/Belgian contribution to ESA's Envisat, provided alternating nadir and limb measurements from August 2002 until April 2012, when contact with the Envisat platform was lost. The nominal spatial resolution of SCIAMACHY was 30×40 km^2 for nadir measurements with global coverage achieved in 6 days. Finally, GOME-2 on MetOp-A [*Munro et al*., 2006] has provided nadir atmospheric observations since October 2006 and is still in operation. Its spatial resolution is 80×40 km^2 in the UV–Visible region, and the extended swath leads to a global coverage in 1.5 days. This GOME-2 sensor is the first of a series of three identical instruments — GOME-2 on MetOp-B was launched in September 2012 and the GOME-2 on MetOp-C is planned for launch in 2018.

In order to meet the aforementioned GCOS requirements, it is crucial that the level-2 total ozone data sets derived from individual sensors show a high level of consistency. To achieve this goal, the CCI multisensor total ozone record uses a common retrieval algorithm applied to all sensors: this is the direct-fitting algorithm GODFIT (GOME-type Direct FITting). This algorithm has a 10-year heritage of development for the GOME instrument, and it has been installed as a core component in the GOME operational system GDP v5 operated at the German Space Agency DLR [*Van Roozendael et al*., 2012]. Independent geophysical validation showed that a direct-fitting approach outperforms the DOAS-type algorithm GDP v4.x previously used for the generation of the operational GOME products [*Lambert et al*., 2012]. Here, we report for the first time, on a combined record of total ozone column retrievals with the latest version 3 of GODFIT applied to the three European sensors GOME, SCIAMACHY, and GOME-2.

Section 2.1 summarizes the main features of the GODFIT algorithm (for more details, this was extensively described in *Van Roozendael et al*. [2012]), while section 2.2 presents the latest developments realized for GODFIT within the Ozone_CCI project. Section 2.3 introduces a new soft-calibration scheme applied to the level-1 reflectances; we show that this scheme reduces the impact of radiometric calibration errors and instrumental degradation in the level-1 products, leading to a significant improvement in intersensor consistency. Section 2.4 discusses the various sources of error on the retrieved ozone column, and gives an estimate of the total error budget. In Section 3, we report on first intersatellite comparison results based on these reprocessed ozone data sets. Section 3 also contains an overview of validation results. A summary of the findings and perspectives is given in Section 4. This paper is the first of a series of three articles on the CCI total ozone ECV. Validation results for these level-2 reprocessed data sets will be discussed extensively in the next article, while the third paper will be dedicated to the construction of a level-3 homogeneous merged data record spanning the period 1996–2011.

2. Total Ozone Retrievals

2.1. The Retrieval Algorithm GODFIT

The GODFIT algorithm is designed to retrieve total ozone columns from earthshine backscattered ultraviolet light spectra measured by space-borne nadir sensors. Based on a direct-fitting methodology, GODFIT is more accurate than the DOAS (Differential Optical Absorption Spectroscopy) approach, especially for scenarios with optically thick atmospheres at high solar zenith angles and/or large ozone columns [*Lambert et al*., 2012]. As a result, GODFIT-derived ozone data exhibit reduced solar zenith angle dependence and smaller seasonality [*Lerot et al*., 2010; *Van Roozendael et al*., 2012]. GODFIT has been recently implemented in the GOME/ERS-2

operational environment GDP v5; the full algorithm is described in *Van Roozendael et al.* [2012]. Here, we give a summary of the main features of the algorithm, with the focus on new developments realized as part of the CCI project described in section 2.2.

GODFIT is based on a standard inverse model, using least-squares minimization of the differences between simulated and measured sun-normalized radiances in the ozone fitting window 325–335 nm. Forward-model simulations are performed on-the-fly with the multiple scatter radiative transfer model LIDORT (LInearized Discrete Ordinate Radiative Transfer) [*Spurr*, 2008]. In addition to total ozone, the state vector includes a temperature-shift parameter, four closure terms, one Ring scaling factor, one Doppler wavelength shift parameter, and in the case of GOME, an additional scaling factor for an undersampling cross section [*Van Roozendael et al.*, 2006]. All Jacobians (partial derivatives of the radiances with respect to the above state vector elements) are calculated analytically as part of the forward model component.

The optical atmosphere must be defined before every iteration step in the retrieval. A key point in this regard is the specification of the ozone profile, which is based on the total ozone column-classified climatology TOMS v8 [*Bhartia and Wellemeyer*, 2002; *McPeters et al.*, 2007]. Profiles are provided for 18 10°-latitude bands, with a classification also on the total column itself. For each new estimate of the total ozone Ω, the appropriate profile is calculated using a simple linear interpolation scheme on the column classification. Ozone profiles are specified in 13 layers ranging from the ground to 0.03 hPa. The representativeness of the tropospheric ozone content has been improved by combining the TOMSv8 climatology with a recent tropospheric ozone column climatology based on OMI and MLS measurements [*Ziemke et al.*, 2011] (see section 2.2.2.).

For the a priori temperature profiles, we use those supplied with the TOMSv8 ozone profile climatology. These T-profiles are uniformly shifted at all levels by an absolute temperature value; this temperature shift (T-shift) is an element of the state vector. Since this T-shift parameter is determined by the ozone absorption structures, the temperatures of the shifted profile are mainly representative of the effective temperature of the ozone absorption, which is strongly weighted toward the ozone maximum. A number of O_3 cross-section data sets have been intercompared in past studies [*Liu et al.*, 2007b; *Lerot et al.*, 2009]. As the baseline for GODFIT, we have chosen the Brion, Daumont, and Malicet (BDM) data set [*Daumont et al.*, 1992; *Malicet et al.*, 1995; *Brion et al.*, 1998] for its accurate wavelength calibration, reliable temperature dependence and high signal-to-noise ratio in the Huggins bands. These high-resolution cross sections have been adjusted to the appropriate spectral resolutions for the three sensors. These "preconvolved" cross sections are based on known slit functions and include the application of a so called "I_0 correction" as described in *Van Roozendael et al.* [2006].

In the inversion, aerosol and surface broadband radiative effects are filtered out by means of a cubic polynomial closure term. The "*internal closure*" mode of GODFIT ensures that the information on the scene reflectivity contained in the closure is coupled with the radiative transfer calculations [*Van Roozendael et al.*, 2012]. The adjusted closure may be interpreted as an effective wavelength-dependent albedo. Such an approach has several advantages. Tropospheric absorbing and scattering aerosols are implicitly accounted for, and simulations do not rely on the ingestion of highly uncertain external aerosol optical property information (see section 2.4). Also, errors due to the incorrect choice of external surface albedo (e.g., at high latitudes where snow coverage from climatologies is not reliable) will be greatly reduced. The drawback of this approach is that it requires an accurate radiometric calibration of the measured spectra (see section 2.3).

The GDP v5 algorithm [*Van Roozendael et al.*, 2012] corrects for clouds using the Independent Pixel Approximation (IPA), treating clouds as Lambertian reflectors with effective parameters provided by the OCRA/ROCINN algorithms [*Loyola et al.*, 2007]. In general, this model works well except in the presence of high clouds, when the retrieved ozone columns tend to be too large by a few percent [*Lambert et al.*, 2012]. To minimize this effect, we have adopted the concept of *effective scene* proposed by *Coldewey-Egbers et al.* [2005]. Radiances are simulated using a single atmospheric scene with an effective surface located at an altitude which is computed as the cloud-fraction weighted mean of the cloud and ground altitudes. The effective albedo of the scene is retrieved simultaneously with the ozone column using the internal closure mode of GODFIT. Although the retrieval is driven by the ozone profile above this effective scene height, the final ozone column corresponds to the integrated profile down to the true surface, including that part of the column between ground and effective scene heights. Effective cloud parameters are consistently supplied for each sensor using the FRESCO v6 algorithm [*Wang et al.*, 2008]. Over snow and ice

scenes, FRESCO cannot retrieve the cloud fraction, but it still provides an effective altitude for the reflecting surface. For such pixels, the effective scene height is set to the FRESCO altitude, and an effective scene albedo is retrieved from GODFIT.

Sun-normalized radiances are calculated with the LIDORT model (section 2.2.1). This is a scalar model that computes radiances in the absence of atmospheric polarization. To account for the spectral structures induced by inelastic scattering processes, an improved semi-empirical Ring correction has been developed — this is presented in section 2.2.3. Correction factors for the polarization are discussed in section 2.2.4.

Simulated spectra are computed on the wavelength grid associated with the daily measurement of the solar irradiance spectrum. To ensure accurate wavelength registration, a recalibration procedure is applied to measured spectra to account for possible wavelength shift and squeeze errors; this procedure is described in *Van Roozendael et al*. [2006] and is based on cross correlation with the high-resolution sun spectrum provided by *Chance and Kurucz* [2010]. In addition, the Doppler effect causes a shift of spectral structures in the earthshine radiances compared to those in the sun spectra; a fitted shift parameter applied to radiances takes care of this effect.

2.2. New Developments for the GODFIT Algorithm

2.2.1. Radiative Transfer Tools

One drawback of the direct-fitting approach is that it requires intensive Radiative Transfer (RT) computational time. Typically, the processing time is one to two orders of magnitude longer than that for DOAS; this depends on the number of wavelengths in the fitting interval. In order to facilitate the applicability of the algorithm to the three sensors in this study, we have used a new accelerated-performance scheme for the GODFIT radiative transfer computations [*Spurr et al*., 2013]. This scheme is based on the application of Principal Component Analysis (PCA) to optical property data sets used for RT simulation — most of the variance in the mean-removed optical data is contained in the first and most important empirical orthogonal functions (EOFs). Thus, full multiple-scattering (MS) computations with LIDORT are done only for the mean profile and the first few EOF optical profiles. These LIDORT MS results are then compared with MS radiances from a 2-stream (2S) RT code [*Spurr and Natraj*, 2011], and a second-order central difference scheme based on these LIDORT/2S difference and on the data Principal Components is then used to provide correction factors to the MS field at every wavelength. Thus, it is only necessary to compute the MS radiances at every wavelength using the much faster 2S code. Single-scatter radiances are computed accurately in a spherically curved atmosphere. This PCA methodology is fully differentiable with respect to all retrieval parameters, so that all necessary Jacobians can be computed accurately, even including the ozone profile Jacobians necessary for the calculation of averaging kernels. As shown in *Spurr et al*. [2013], this method leads to time saving of factor 4 for total ozone retrieval when the first two EOFs are used, while maintaining excellent accuracy throughout.

2.2.2. Tropospheric Ozone Climatology

Nadir UV–Visible space-borne sensors show poor sensitivity to the lowermost layers of the atmosphere [*Van Roozendael et al*., 2012]. Thus, a priori knowledge of the tropospheric ozone content is very important for accurate total ozone retrieval, especially in cloud-contaminated scenes. For the monthly 18-latitude O_3 profile TOMS v8 climatology [*Bhartia and Wellemeyer*, 2002; *McPeters et al*., 2007] used in GODFIT, longitudinal dependence of the profile shape is not explicitly considered. Although total ozone has been shown to be a good proxy for the stratospheric profile shape [*Wellemeyer et al*., 1997], in the troposphere, other factors explain the longitudinal variation of the ozone content. In tropical regions, zonal asymmetries are caused by dynamics and local biomass burning events [*Ziemke et al*., 1996]. As a result, the longitudinal dependence of tropospheric ozone in Southern Tropics follows a wave-one pattern with a maximum close to 0° of longitude and a minimum around 180°. In other latitude regions, the tropospheric ozone content may locally vary because of air quality issues (e.g., *Dentener et al*., 2006).

Recently, a tropospheric ozone column climatology based on a combination of OMI and MLS measurements has been generated by *Ziemke et al*. [2011]. This climatology provides monthly mean tropospheric columns with a spatial resolution of 1° × 1.25° (latitude × longitude) for latitudes from 60°N to 60°S. Tropopause heights are also provided with this climatology. The tropospheric climatology is applied as follows. First, we scale the tropospheric part of the TOMSv8 profile so that the integrated tropospheric profile matches the

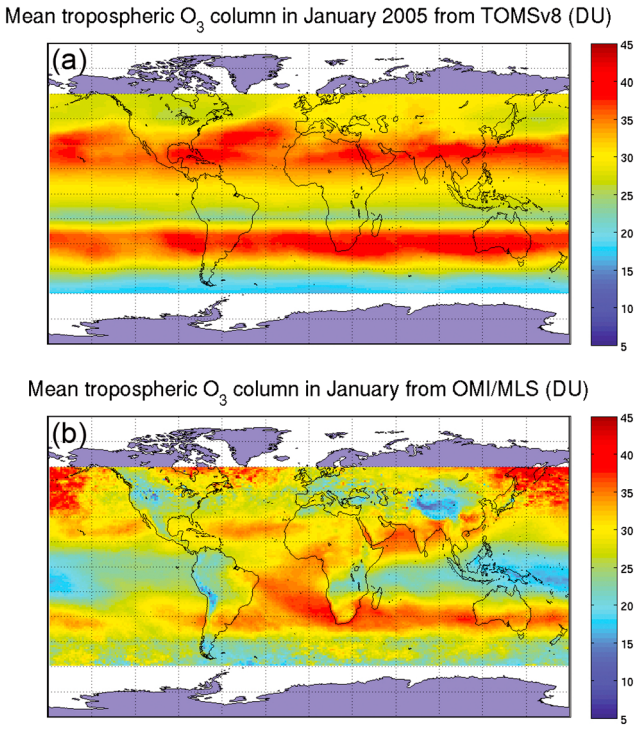

Figure 1. Comparison of mean tropospheric columns in January, from the (a) TOMSv8 and (b) OMI/MLS climatologies.

tropospheric column from the OMI/MLS climatology. Then, the stratospheric part of the profile is also scaled in order to maintain the correspondence between the total column and the integrated profile. Figure 1 compares the tropospheric O_3 columns from the TOMSv8 and the OMI/MLS climatologies in January. Strong longitudinal variations are clearly present in the OMI/MLS tropospheric ozone columns. The small zonal changes visible in the TOMSv8 columns are caused by variations in the Tropopause altitude. Using this tropospheric climatology leads to differences in the retrieved total ozone in Tropical Regions up to 1% for clear scenes and up to 3% for highly cloud-contaminated pixels.

2.2.3. Semi-Empirical Ring Correction

Inelastic Rotational Raman Scattering (RRS) by molecular oxygen and nitrogen is responsible for the filling-in of Fraunhofer lines and molecular absorption signatures in backscattered light spectra recorded by satellite UV–Vis sensors. This so-called Ring effect, first observed for skylight spectra by *Grainger and Ring* [1962], introduces high-frequency structures in the measured radiances; these structures need to be taken into account in retrievals of atmospheric trace gases. For optically thin trace gas absorption, the Ring effect is generally well corrected when it is treated as a pseudo-absorber in DOAS retrievals. Ring spectra are usually computed by convolution of a high-resolution solar atlas (e.g., *Chance and Kurucz*, 2010) with RRS cross sections [*Chance and Spurr*, 1997].

However, for accurate total ozone retrievals in the Huggins bands, the filling-in of telluric absorption features also needs to be accounted for. It has been shown [*Van Roozendael et al*., 2002] that the neglect of this effect can lead to underestimation of the total column by up to 10%. The DOAS-based GOME Data Processor (GDP) v4 includes a Molecular Ring correction applied to the effective O_3 slant column before the conversion to the total vertical column [*Van Roozendael et al*., 2006]. In the most recent GDP v5 processor based on direct fitting, a Ring spectrum with adjustable amplitude is added to the sun-normalized intensity simulated by LIDORT [*Van Roozendael et al*., 2012]. This Ring spectrum is calculated using a formulation accounting for the smoothing of both solar and telluric lines. Although this formulation is sufficiently accurate in most circumstances, there are some limitations for particular conditions:

1. The O_3 absorption of the inelastically scattered light is represented through the use of simple geometrical enhancement factors — these may not be accurate enough at large solar and viewing angles.
2. The loss of photons due to inelastic scattering at a given wavelength has been neglected. This is mostly compensated by the closure-term filter for broadband signatures. However, information on the reflectivity of the scene derived from this closure could be biased, and this will lead to small errors on the retrieved O_3 column (see Figure 5).

Modern radiative transport models such as LIDORT-RRS [*Spurr et al*., 2008] can accurately simulate the nadir backscattered radiance field including both elastic and inelastic RRS processes. However, such RT models are computationally expensive and thereby inappropriate for processing large amount of data with online simulations. Instead, we have developed a semi-empirical formulation to calculate filling-in factors, which, once multiplied to the elastically scattered radiances, correct them for the structures introduced by the inelastic processes. This formulation closely reproduces the filling-in factors calculated by LIDORT-RRS and is based on

concepts developed by *Wagner et al.* [2009], but also includes additional treatment of atmospheric absorption effects.

As a starting point, we consider equation (2) of *Wagner et al.* [2009]:

$$R_{\mathrm{tot}}(\lambda) = R_{\mathrm{el}}(\lambda) + R_{\mathrm{inel,in}}(\lambda) - R_{\mathrm{inel,out}}(\lambda). \tag{1}$$

Here, R_{tot} is the spectral radiance, R_{el} the elastic radiance under the assumption that all photons are elastically scattered, and $R_{\mathrm{inel,in}}$ and $R_{\mathrm{inel,\ out}}$ are source and loss terms due to inelastic scattering. Taking into account the ozone absorption, these last three terms may be written:

$$\begin{aligned} R_{\mathrm{el}}(\lambda) &= T_{\mathrm{el}} F_0(\lambda) \exp(-\tau_{O_3}(\lambda)) \\ R_{\mathrm{inel,out}}(\lambda) &= T_{\mathrm{inel}} F_0(\lambda) \exp(-\tau_{O_3}(\lambda)) \\ R_{\mathrm{inel,in}}(\lambda) &= T_{\mathrm{inel}} \int F_0(\lambda') P(\lambda,\lambda') \exp\left(-\tau_{O_3,\mathrm{in}}(\lambda')\right) d\lambda' \exp\left(-\tau_{O_3,\mathrm{out}}(\lambda)\right). \end{aligned} \tag{2}$$

In these expressions, T_{el} and T_{inel} are the atmospheric transmissions for elastically and inelastically scattered photons, respectively. The ratio $\rho_0 = \frac{T_{\mathrm{inel}}}{T_{\mathrm{el}}}$ represents the rotational Raman scattering probability, which is assumed to be wavelength-independent in the (relatively small) ozone fitting window. F_0 is the solar irradiance, $P(\lambda,\lambda')$ is the probability for a photon to be inelastically scattered from wavelength λ' to λ, and τ_{O_3}, $\tau_{O_3,\mathrm{in}}$, and $\tau_{O_3,\mathrm{out}}$ are the ozone optical densities for the total light path and for the light paths from the satellite to the surface (incoming) and vice versa (outgoing). In addition to the assumptions described in *Wagner et al.* [2009], we also consider that inelastic scattering occurs close to the surface.

$R_{\mathrm{inel,in}}$ can easily be reformulated as:

$$R_{\mathrm{inel,in}}(\lambda) = T_{\mathrm{inel}} F_0(\lambda) \sigma_{\mathrm{ring}}(\lambda) \exp\left(-\tau_{O_3,\mathrm{out}}(\lambda) - CA_{\mathrm{in}}(\lambda)\sigma_{O_3}^{\mathrm{RRS}}(\lambda)\right), \tag{3}$$

where C is the total ozone column, A_{in} is a geometrical enhancement factor for incoming light that is assumed to have limited wavelength dependence, and the cross sections $\sigma_{\mathrm{ring}}(\lambda)$ and $\sigma_{O_3}^{\mathrm{RRS}}(\lambda)$ are defined as:

$$\begin{aligned} \sigma_{\mathrm{ring}}(\lambda) &= \frac{\int F_0(\lambda') P(\lambda,\lambda') d\lambda'}{F_0(\lambda)}, \\ \sigma_{O_3}^{\mathrm{RRS}}(\lambda) &= \frac{\int F_0(\lambda') P(\lambda,\lambda') \sigma_{O_3}(\lambda') \mathrm{d}\lambda'}{\int F_0(\lambda') P(\lambda,\lambda') d\lambda'}, \end{aligned} \tag{4}$$

with σ_{O_3} a typical ozone absorption cross section. The Ring cross section σ_{ring} and the RRS-smoothed O_3 cross section $\sigma_{O_3}^{\mathrm{RRS}}$ can be generated through convolution of normalized Raman scattering cross sections with a solar reference spectrum on the one hand [*Wagner et al.*, 2009] and with a solar reference spectrum multiplied by a typical ozone absorption cross section on the other hand. Examples of such cross sections are shown in Figure 2. Note that the expression for $R_{\mathrm{inel,in}}$ is similar to the Ring term added to the elastic radiance in the GDP v5 algorithm; as noted above, the loss term $R_{\mathrm{inel,out}}$ has been neglected in GDPv5.

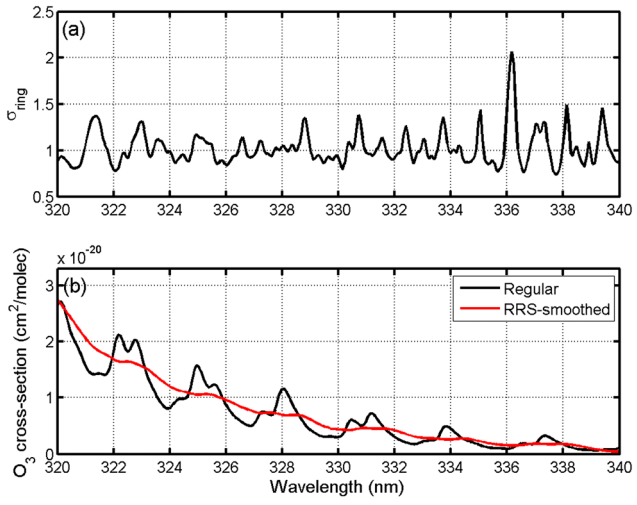

Figure 2. Illustration of typical cross sections used in the semi-empirical Ring formulation in the interval 320–340 nm. (a) The Ring cross section σ_{ring} shows structures induced by filling-in of Fraunhofer lines due to inelastic scattering. (b) Comparison of a regular O_3 cross section with the RRS-smoothed O_3 cross section $\sigma_{O_3}^{\mathrm{RRS}}$ at 243°K. All cross sections plotted here have been adjusted to the GOME/ERS-2 spectral resolution.

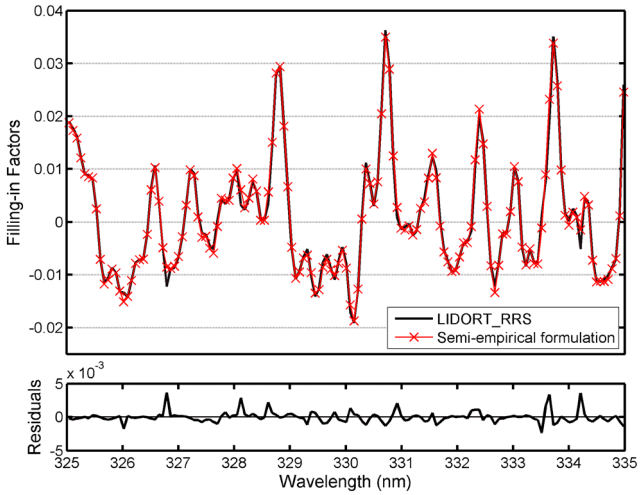

Figure 3. Comparison of filling factors computed using LIDORT-RRS against those derived from the semi-empirical formulation in the ozone fitting window. These spectra have been calculated for a total ozone column of 300 DU and a surface albedo of 0.06. The solar and viewing zenith angles are 40° and 30° and the relative azimuth angle is 10°.

Combining equations (1), (2), and (3), the sun-normalized radiance (defined as $R_n = \frac{R_{tot}}{F_0}$) may be written as:

$$R_n(\lambda) = \frac{R_{el}(\lambda)}{F_0(\lambda)}\left\{1+\rho_0\left[\sigma_{ring}(\lambda)\exp\left(-\tau_{O_3,out}(\lambda)-CA_{in}(\lambda)\sigma^{RRS}_{O_3}(\lambda)+\tau_{O_3}(\lambda)\right)-1\right]\right\} \quad (5)$$

This result defines the filling-in factors *FF(λ)*:

$$R_n(\lambda) = \frac{R_{el}(\lambda)}{F_0(\lambda)}\{1+FF(\lambda)\} \quad (6)$$

The various optical density terms τ in the filling-in factors *FF(λ)* may be expressed in terms of effective air mass factors A_{tot}, A_{in}, and A_{out} representative of the total, incoming, and outgoing light paths, respectively. We can then write:

$$FF(\lambda) = \rho_0\left[\sigma_{ring}(\lambda)\exp\left(-\tau^{v}_{O_3}(\lambda)A_{out}(\lambda)-\tau^{RRS,v}_{O_3}(\lambda)A_{in}(\lambda)+\tau^{v}_{O_3}(\lambda)A_{tot}\right)-1\right] \quad (7)$$

with $\tau^{v}_{O_3} = \sum_{i=1}^{n} C_i\sigma_{O_3}(T_i)$ and $\tau^{RRS,v}_{O_3} = \sum_{i=1}^{n} C_i\sigma^{RRS}_{O_3}(T_i)$, where C_i is the O_3 partial column in layer *i*, and the cross sections are interpolated to the appropriate layer-average temperature T_i. A_{tot} is easily calculated with the RT model at one reference wavelength (i.e., 325 nm) while A_{in} and A_{out} are assumed to vary linearly over the ozone fitting window. When ρ_0, A_{in}, and A_{out} are adjusted, the filling-in factors based on equation (7) reproduce very closely those calculated with LIDORT-RRS, as illustrated in Figure 3. On this basis, look-up tables (LUT) of A_{in} and A_{out} have been generated for a range of conditions based on representative observation angles, total ozone columns (and associated typical midlatitudes profiles), surface albedos, and altitudes (see Table 1). Typical dependencies for these two AMF parameters are shown in Figure 4. In practice, a slope parameter is also tabulated in addition to the effective AMF at 325 nm; this slope parameter accounts for a possible linear wavelength dependence within the ozone fitting window. With these two parameters, the effective AMFs can easily be computed at any wavelength in the interval 325–335 nm.

In total ozone retrievals, the filling factor spectrum can be computed easily for every iteration using equation (7), with the appropriate effective air mass factors extracted from the LUTs. The RRS probability ρ_0 is an element of the retrieval state vector. In theory, this parameter could also be tabulated as with A_{in} and A_{out}, but in practice, allowing it to be fitted gives better results because of its high sensitivity to scene reflectivity and cloud parameters.

Figure 5 contrasts total ozone errors according to the level of approximation in the Ring formulation; errors are plotted as a function of the solar zenith angle. For this example, synthetic radiances were generated using LIDORT-RRS for an atmosphere with 300 DU total ozone, and a surface albedo of 0.06. The retrieval algorithm, including an empirical formulation to correct the LIDORT elastic radiances for the Ring effect, is then applied to these simulated spectra. The difference between the retrieved and the "true" ozone column gives an estimate of the error due to the Ring formulation. The black and blue curves show (respectively, for constant and quadratic closure terms) the errors incurred when the loss term due to inelastic scattering is neglected. In practice, the closure polynomial is always second order or

Table 1. Classification Grids for the Effective Air Mass Factors A_{in} and A_{out}

Dimension	Grid
Total ozone (DU)	[200 300 400]
SZA (degrees)	[20 30 40 50 60 70 75 80 85 88 90]
VZA (degrees)	[0 20 40 60]
RAA (degrees)	[0 30 60 90 120 150 180]
Surface albedo	[0.02 0.05 0.1 0.3 0.5 0.7 0.8 0.9]
Surface altitude (km)	[0 2 4 6 8 10 12 14 16]

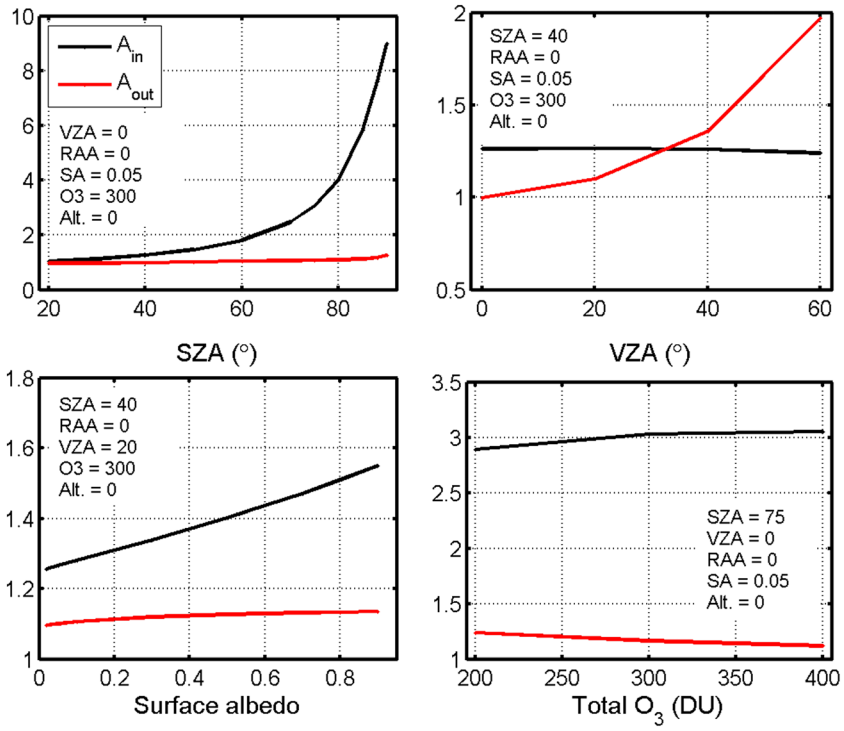

Figure 4. Illustration of the dependencies of the effective air mass factors A_{in} and A_{out} at 325 nm with respect to solar and viewing zenith angles (upper left and upper right panels), and to total ozone and surface albedo (lower left and lower right panels). In each panel, parameters that were kept fixed in these tests are indicated as inserts.

more, and therefore the blue curve is representative of the errors in the GDPv5 algorithm. The red curve corresponds to the new semi-empirical Ring correction, leading to negligible errors. Note that these errors remain small in extreme conditions. For example, a scenario with an ozone column of 500 DU, a surface albedo of 0.8, and a solar zenith angle larger than 85° leads to errors less than 0.5%.

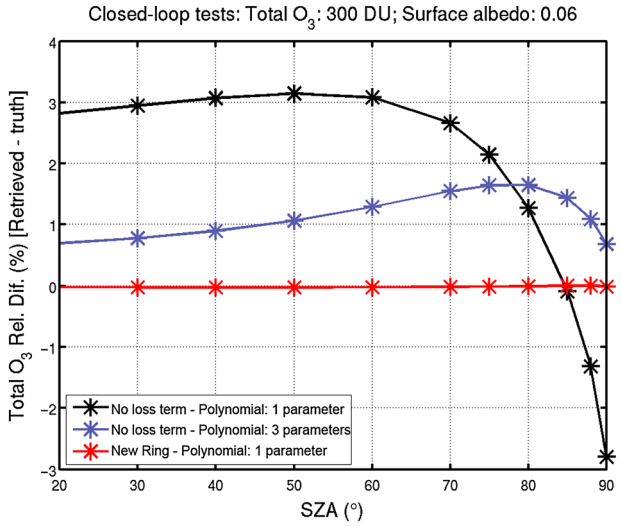

Figure 5. Total ozone relative errors due to different levels of approximation in the Ring formulation, as plotted against the solar zenith angle. Synthetic spectra are generated using LIDORT-RRS and retrievals are performed using elastic radiances corrected for the Ring effect. The black and blue curves show errors induced from neglect of the inelastic scattering "loss term"; the red curve shows negligible error using the new semi-empirical Ring correction. These closed-loop tests were carried out for total ozone 300 DU and surface albedo 0.06.

2.2.4. Polarization Correction

In classical DOAS algorithms and also in GDP v5 [*Van Roozendael et al.*, 2012], polarization signatures are taken to be smooth functions of wavelength and are subsumed in the polynomial closure. The vector RT model VLIDORT [*Spurr*, 2008] can simulate backscattered radiances with polarization included; the VLIDORT model is fully compatible with the scalar LIDORT code. A vector-scalar radiance comparison between the two codes shows systematic differences to the level of a few percent; these depend on the observation geometry, the surface albedo and altitude, and also on ozone absorption itself [*Mishchenko et al.*, 1994]. Although these differences generally show little variation over the ozone fitting window, spectral structures may become

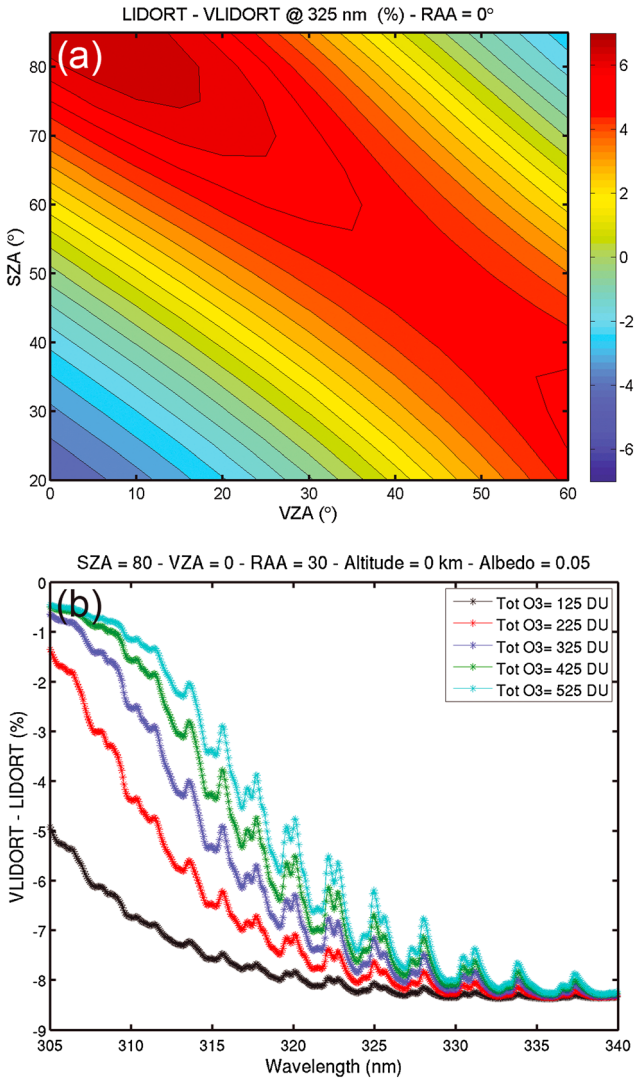

Figure 6. (a) Relative percentage differences between the TOA radiances simulated with LIDORT (no polarization) and VLIDORT (with polarization) at 325 nm plotted against the SZA and VZA; the RAA is 0°, the surface albedo is 0.05 and the ozone absorption is neglected. (b) VLIDORT/LIDORT relative differences in TOA radiances as a function of wavelength, at large SZA 80°, for different total ozone columns; the other parameters are RAA = 30°, VZA = 0°, and surface albedo 0.05.

significant in a scenario with high ozone optical density, at large solar zenith angle and/or with high ozone column.

Figure 6a illustrates the impact of atmospheric polarization on radiances simulated at 325 nm, contour plotted with the solar and viewing zenith angles, for a surface albedo of 0.05, and without any ozone absorption. This figure corresponds to a relative azimuth angle (RAA) of 0°; it is the case that SZA and VZA dependencies change significantly for other RAA values. Figure 6b also shows the impact of polarization on the radiances as a function of wavelength, for SZA 80° and for different ozone amounts. Spectral structures associated with ozone absorption are evident for these higher ozone optical densities. Such structures cannot be included in the closure polynomial. In addition, the scene albedo derived from this closure term will be biased if atmospheric polarization is not accounted for.

Ideally, a vector code such as VLIDORT should be used in the forward model. However, to minimize the computational burden with GODFIT, polarization correction factors are applied to simulated scalar radiances. These factors are extracted from a look-up table of VLIDORT-LIDORT intensity relative differences. This LUT provides correction factors at 0.07 nm resolution in the spectral interval 305–340 nm; correction factors are classified according to ranges of the solar zenith, viewing zenith, and relative azimuth angles, surface altitude, ground albedo, and the total ozone column (see Table 2).

2.3. Soft-Calibration of Reflectances

Although a common group of retrieval settings is applied consistently to all three level-1 data sets from GOME, SCIAMACHY, and GOME-2, systematic differences between the individual total ozone data sets remain. This is seen in Figure 7, where the mean total ozone satellite/Brewer differences based on 8 European stations are plotted as a function of the time. Satellite ozone results are obtained using GODFIT applied to the raw level-1 data sets of GOME, SCIAMACHY, and GOME-2 (v4.0x, v7.04, and v5.12, respectively). As can be seen, the GOME ozone columns agree well with the Brewer data in the first years of operation, but the agreement tails off in later years (dashed red line). It will be shown

Table 2. Classification Grids for Polarization Correction Factors

Dimension	Grid
Total ozone (DU)	[125 175 225 275 325 375 425 475 525 575]
SZA (degrees)	[20 30 40 50 60 70 75 80 85]
VZA (degrees)	[0 10 20 30 40 50 55]
RAA (degrees)	[0 30 60 90 120 150 180]
Surface albedo	[0. 0.05 0.1 0.2 0.3 0.5 0.8 1.]
Surface altitude (km)	[0 5.51 10.32 14.71]

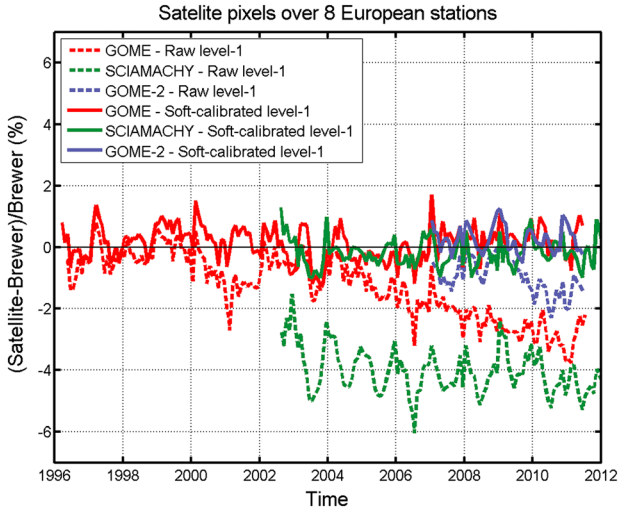

Figure 7. Monthly mean satellite-Brewer O_3 column relative differences, based on eight Northern midlatitude stations, plotted as a function of time. The dashed lines correspond to satellite retrievals derived from the original level-1 data. The solid lines show the improved consistency with the Brewer when soft-calibrated level-1 data are used.

below that this effect mainly originates from a bias in the retrieved effective albedo caused by instrumental degradation. The SCIAMACHY-Brewer differences are characterized by strong seasonality around a mean low bias of −4% (dashed green curve). The GOME-2 O_3 columns are slightly lower than the Brewer values up to late 2009, when the throughput tests [*Lang*, 2012] resulted in a further decrease of the columns (dashed blue curve). These patterns are likely due to systematic radiometric errors and degradation effects affecting the measured level-1 reflectances.

To deal with these patterns and enhance the intersensor consistency, a soft-calibration scheme has been developed. Similar procedures have been successfully applied in the past to improve the absolute radiometric calibration of space-borne instrument spectra, in the context of O_3 and SO_2 profile retrievals, and for absorbing aerosol index retrieval [*van der A et al.*, 2002; *Liu et al.*, 2007a; *Tilstra et al.*, 2012; *Cai et al.*, 2012]. Our total ozone retrievals are sensitive not only to absolute radiometric calibration errors (a feature inherent in the fitting of effective albedo) but also to the presence of high-frequency spectral features that may interfere with the ozone absorption. The soft-calibration procedure developed here accounts for both these aspects. As with previous studies, the calibration procedure relies on comparisons of measured level-1b reflectances to simulated values in the spectral interval 325–335 nm, the simulations being performed with the same forward model as that used for the retrievals. Since we aim at correcting for spectral features in the measured spectra, it is of paramount importance to select a reference ozone record as the major input to the simulations. An additional requirement in the present paper is to ensure that such a reference ozone record spans the combined lifetimes of the three instruments, i.e., GOME/ERS-2, SCIAMACHY/Envisat, and GOME-2/MetOp-A. Brewer direct-sun ozone column measurements from carefully chosen reference stations do offer such a long time series of ozone observations of sufficient quality for the detection of possible artifacts in the satellite reflectances. An obvious drawback of this choice is the introduction of a dependence on the Brewer observations themselves. To avoid this problem as much as possible, we have selected a very limited set of reliable stations, all located in Europe (listed in Table 3). Another problem with our procedure arises from the limited number of collocations between the satellite and the Brewer instruments; this is especially the case for GOME and SCIAMACHY, and the main effect is to prevent filtering for cloud contaminated pixels. In future, we will investigate other possible choices of reference observations in order to avoid these drawbacks.

2.3.1. Simulations and Identification of Level-1 Issues

Figure 8 illustrates the basic concept of the soft-calibration scheme. For each satellite observation in collocation (i.e., within a radius of 300 km) with a suitable reference Brewer ozone measurement, a simulated reflectance is computed using the forward model of GODFIT. The ratio of simulated and measured level-1 reflectances contains both the low- and high-frequency discrepancies. These are separated by fitting a low-order polynomial through the ratio (Figure 8). In the following, we will name the low-frequency differences "absolute

Table 3. List of Reference Brewer Instruments Considered for the Soft-Calibration Scheme

Stations	Coordinates (Lat., Lon.)
Arosa (Switzerland)	46.78°N, 9.68°E
Budapest Lorinc (Hungary)	47.43°N, 19.18°E
De Bilt (The Netherlands)	52.10°N, 5.18°E
Hohenpeissenberg (Germany)	47.80°N, 11.02°E
Hradec Králové (Czech Republic)	50.18°N, 15.83°E
Madrid (Spain)	40.46°N, 3.65°W
Thessaloniki (Greece)	40.65°N, 22.90°E
Uccle (Belgium)	50.80°N, 4.35°E

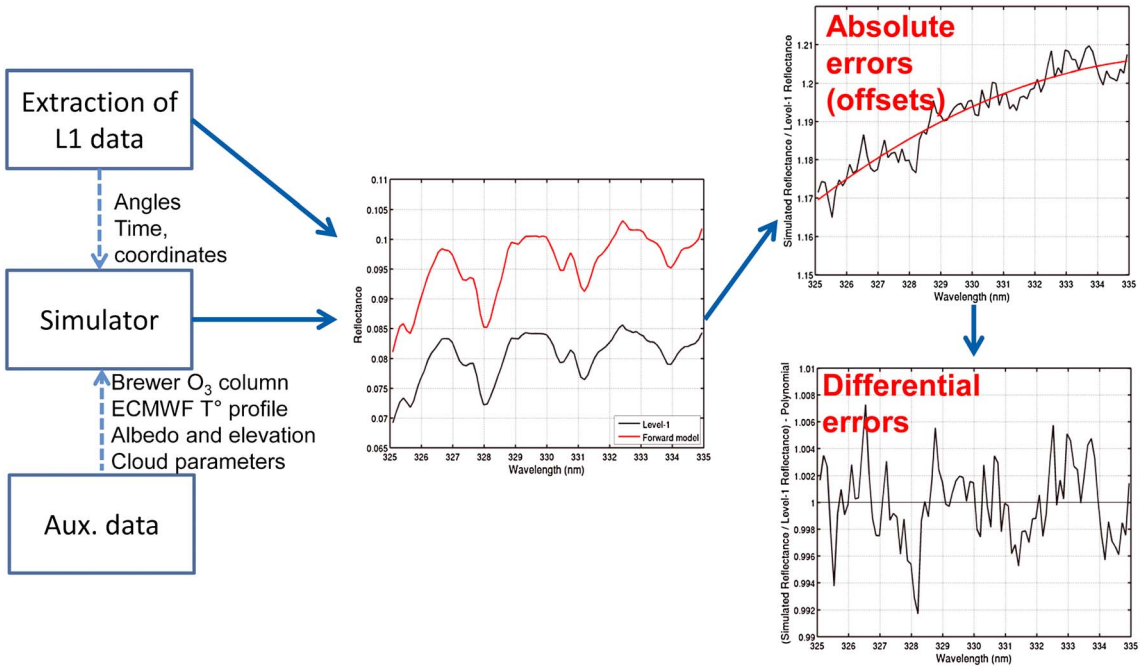

Figure 8. Sketch illustrating the possible detection of radiometric calibration (absolute) errors and artificial spectral features (differential errors). For each satellite scene in colocation with a Brewer measurement, a simulated spectrum is compared to the level-1 reflectance. A low-order polynomial fitted through the ratio of the spectra discriminates broadband effects from the high-frequency features.

errors," while the high-frequency differences are referred to as "differential errors." This process is repeated for hundreds of thousands of spectra, so that the resulting statistics are sufficient to reduce as much as possible the errors due to noise, due to spatial ozone gradients, or associated with model input parameters used in the simulations.

As noted already, the simulations are performed using the same forward model as that used in the retrievals. This produces an advantageous cancellation of errors associated with the forward model itself. One difference with respect to the retrieval mode is that the scene reflectivity has to be fixed. In the simulations, we use the independent pixel approximation (IPA) comprising an intensity-weighted mean of the radiances simulated for the clear and the cloudy parts of the pixels. The surface albedo is extracted from the OMI surface reflectance climatology [*Kleipool et al.*, 2008]. Clouds are assumed to be Lambertian surfaces with parameters provided by FRESCO v6 (as in the retrieval mode). Previous validation exercises have shown that this IPA model works generally well, except in case of very high clouds [*Lambert et al.*, 2012]. However, the occurrence of such high clouds is very low, especially over Europe. The vertical distribution of ozone is extracted from the TOMS v8 climatology combined with the OMI/MLS tropospheric climatology (the same situation as for the ozone retrieval), with the correct profile selected according to the time and the geographical coordinates associated with the corresponding satellite pixel and the reference Brewer ozone column (data here provided by the World Ozone and Ultraviolet Radiation Data Centre Archive). Temperature profiles are taken from the ERA-Interim ECMWF (European Centre for Medium-Range Weather Forecasts) reanalyses [*Dee et al.*, 2011].

Since our focus is on detecting and quantifying artificial spectral features in the ozone fitting interval, it is crucial that measured level-1 spectra are treated exactly as they would be in the retrieval mode, before comparison with simulated values. In particular, the wavelength grids of the recorded spectra are recalibrated as noted in section 2.1. Also, an adjusted wavelength shift is applied to the level-1 radiance in order to account for the Doppler misalignment between the earthshine and solar spectra.

2.3.1.1. Absolute Errors of the Level-1 Reflectances

Figure 9 shows monthly averages of the ratio of satellite to simulated reflectances at 335 nm for the three sensors. Ranges of viewing zenith angles are plotted in different colors. For all instruments, a significant seasonal cycle is evident, which depends on the viewing zenith angle. Interpretation of this seasonality should be made with care. It is also worth noting that the reflectance itself depends strongly on the solar and viewing angles. This

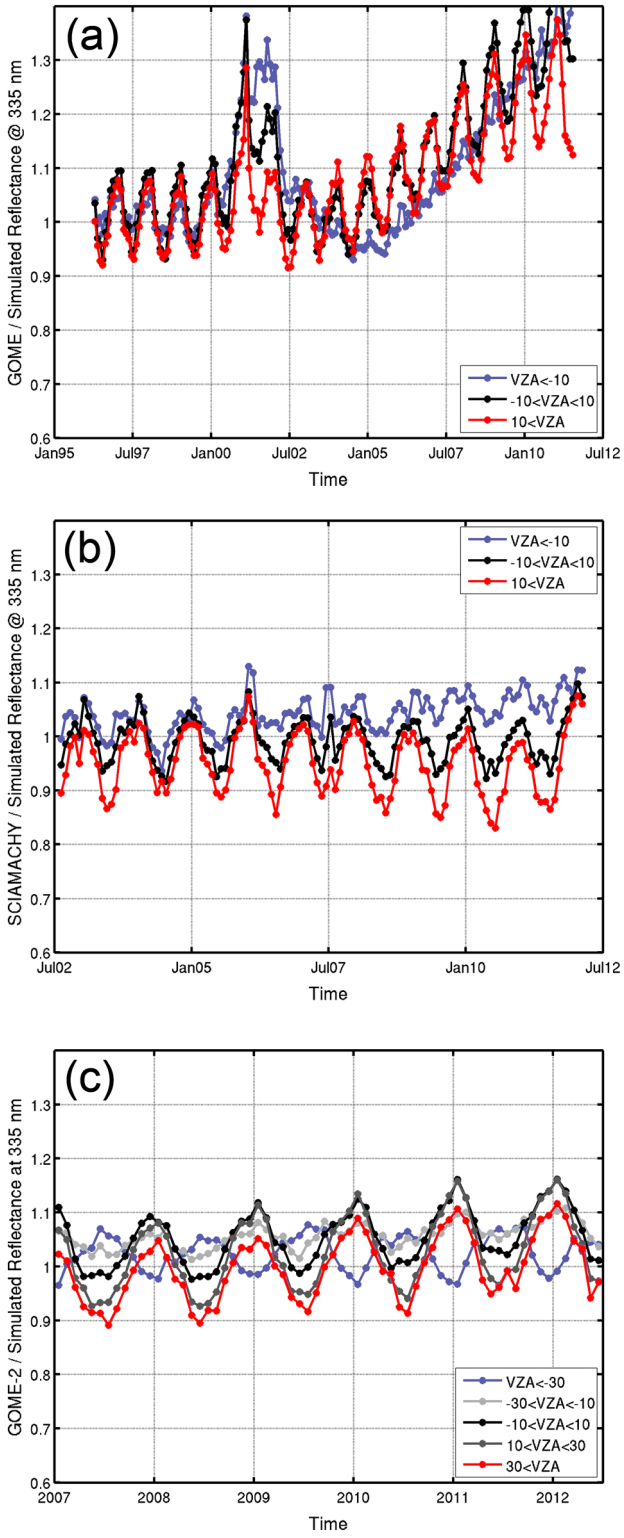

Figure 9. Monthly mean satellite versus simulated reflectance ratios at 335 nm, as a function of time, for GOME (panel (a)), SCIAMACHY (panel (b)) and GOME-2 (panel (c)). The different curves represent different ranges of viewing zenith angle. Negative viewing angles correspond to Eastern pixels and positive angles to Western pixels.

seasonal cycle and its viewing angle dependence likely originate from both instrumental and forward model limitations. Regarding the latter aspect, it has been shown by *Tilstra et al.* [2012] that for SCIAMACHY, reflectances simulated using the IPA may differ from measured values when the cloud contamination is non-negligible — this is especially the case for the "Western" pixels. Also, aerosols are neglected in the forward model. Any natural cycle in the atmospheric aerosol content at the reference sites could impact this reflectance ratio. Since it is very difficult to discriminate instrumental effects from forward model uncertainties, sensitivity tests have been performed to assess the impact on total ozone retrievals of correcting measured reflectances for this seasonal cycle. In general, this effect is less than 0.5%, though it may reach 1% in extreme conditions (clear-sky scenes with large surface albedo). These numbers represent the maximum total ozone error due to the correction of the seasonal cycle if the latter originates entirely from forward model limitations affecting specifically the regions where the reference stations are localized (clouds, aerosols,…). This has been accounted for in the total ozone error budget (see section 2.4).

For the GOME case, it is clear that the instrument has suffered from significant scan-angle dependent degradation over the period 2000–2002 and again from 2005 onward. Detecting such a degradation in the reflectances implies that the radiance and irradiance spectra are impacted differently. *Snel* [2000] attributed such degradation to a change in optical properties of the scan mirror as a result of a contaminant deposit. Previous studies have already focused on the GOME degradation for limited time periods [*Krijger et al.*, 2005; *Liu et al.*, 2007a; *Coldewey-Egbers et al.*, 2008]. Our findings are qualitatively and quantitatively consistent with their results.

SCIAMACHY reflectances appear to be less affected by instrumental degradation. However, it must be remembered that instrumental degradation correction factors (the so-called m-factors) have

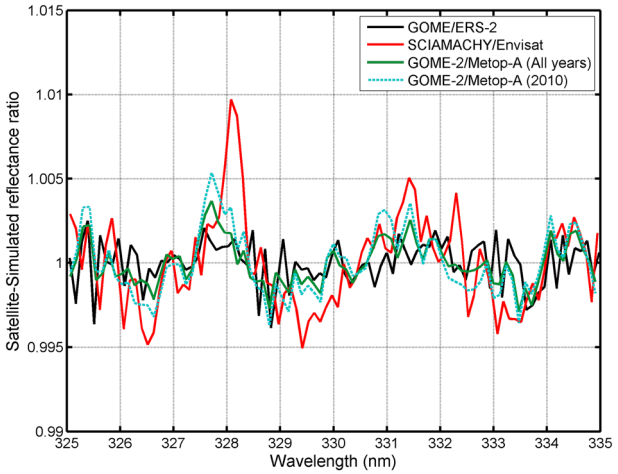

Figure 10. Mean spectral residuals in the satellite/simulation reflectance ratios. These residuals are mean values for all comparison pairs, averaged over all observation geometries and over the full mission time series. SCIAMACHY (red curve) shows larger spectral features in the residuals than does GOME (black curve) and GOME-2 (green curve). The spectral features for GOME-2 are slightly larger after the 2009 throughput tests (cyan curve).

been applied in the level-1 calibration [*Bramstedt*, 2008]. These m-factors do not account for the scan-angle dependence. Interestingly, the different curves in Figure 9 corresponding to Eastern, Western, and nadir pixels diverge from each other over time. This issue has been tackled as part of the ESA's *SCIAMACHY Quality Working Group*, in charge of the improvement of the operational product quality, and it is expected that there will be an improved treatment of degradation in the next version of the level-1 data; this new model will couple the m-factors to a model accounting for a possible contamination of the scan-mirror [*Snel and Krijger*, 2009]. It will be interesting to see if the currently observed scan-angle dependencies are reduced after application of these new m-factors.

Despite a shorter time series, a slight drift is evident in the GOME-2 measured to simulated reflectance ratio (a few percent over 5.5 years, for all VZAs). This is consistent with the analysis of *Cai et al*. [2012] as applied to data from the 3 first years of operation, despite different versions of the level-1 data sets. Comparing directly the reflectance ratio with their results is not trivial, because their simulations rely on a cloud fraction derived from the uncorrected reflectances at 347 nm. This means that their reflectance ratio does not necessarily represent the accuracy of the absolute reflectance [*Cai et al*., 2012].

2.3.1.2. Differential Errors of the Level-1 Reflectances

Once the smooth component of the satellite/simulated reflectance ratio has been filtered out, it becomes possible to identify artificial spectral features in the reflectances. Such features may have a significant impact on total ozone retrievals, depending on their amplitude and spectral shape. The mean satellite/simulated spectral residuals are shown for GOME, SCIAMACHY, and GOME-2 in Figure 10. It is clear that SCIAMACHY residuals are much larger than those for GOME or GOME-2, and this explains the large bias in the SCIAMACHY columns compared to Brewer measurements (see Figure 7 and *Lerot et al*. [2009]). After the throughput test carried out in late 2009, GOME-2 also shows enhanced spectral features, explaining the increased bias (see Figure 7 and *Koukouli et al*. [2012]). The smallest spectral residuals are observed with GOME, and most importantly, they are very stable with time over the full duration of the instrument mission. These results are totally consistent with previous analyses on the stability of the GOME instrument for DOAS-type ozone retrievals (e.g., *Balis et al*., 2007b).

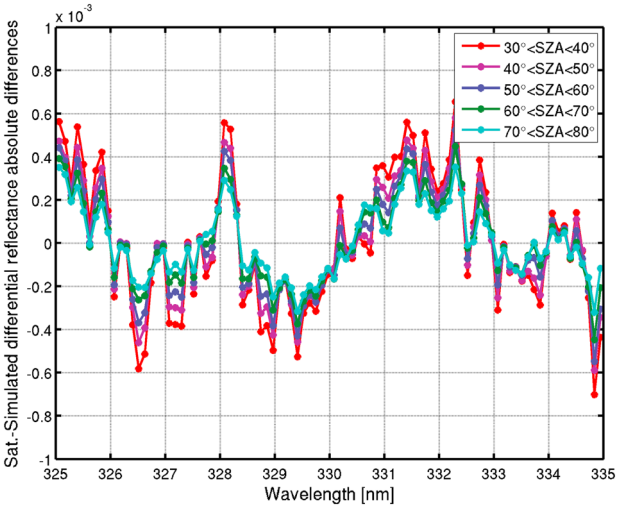

Figure 11. SZA dependence of the differences between the measured SCIAMACHY and simulated differential reflectances.

Interpreting residual spectral features and their possible origins is a challenging task beyond the scope of the present paper. However, the SCIAMACHY anomaly appears to be strongly dependent on season and SZA (see Figure 7 and *van der A et al*. [2010]). Figure 11 shows the absolute differences between the spectral structures from the SCIAMACHY and simulated reflectances for different SZA bins. The

Table 4. Classification Grids for the Reflectance Spectral Correction Factor LUTs for Each Sensor[a]

	Time	SZA	VZA
GOME/ERS-2	1996 – 2011 (1)	30 – 70 (20)	−20 – 20 (20)
SCIAMACHY/Envisat	2003 – 2011 (1)	25 – 85 (10)	−20 – 20 (20)
GOME-2/MetOp-A	2007 – 2012 (1)	25 – 85 (10)	−50 – 50 (10)

[a]The two first numbers represent the lower and upper grid limits (years or degrees); the number in parentheses gives the grid interval. These correction factor spectra are computed for the range 325–335 nm at an interval of ~0.12 nm.

magnitude of these structures clearly decreases at higher SZA. Such a SZA dependence could suggest that the level-1 reflectance artificial structures originate from radiance radiometric errors with an additive component.

2.3.2. Application of Soft Calibration

Look-up tables (LUTs) of spectral correction factors have been constructed for all three sensors using all computed satellite/simulation reflectance ratios. These LUTs have four dimensions: one for the wavelength, one for the time, and two for the viewing and solar zenith angles. The grids of the LUTs have been optimized for each instrument (see Table 4) to account for their own specificities (observation geometry, spatial sampling, etc.). The LUT has a coarse time resolution; consequently, possible seasonal variations are accounted for by the solar zenith angle dimension. Before the total ozone retrieval, the level-1 reflectance is multiplied by a correction factor spectrum interpolated from the appropriate LUT.

In practice, the smooth and absolute components of the correction factors are applied separately. One reason for this is that, for GOME, the LUT of spectral feature corrections has no time dependence, this instrument being very stable over its lifetime. This fact allows us to maintain GOME as the stability reference for the data merging in level-3 algorithms. In addition, as discussed above, the SCIAMACHY differential artificial structures might originate from additive error. This implies that the associated correction factors would also depend slightly on the ozone column itself, as well as on the SZA and VZA (other dependencies are assumed to be negligible).

Adding a fifth dimension to the LUTs to account for this dependence is not trivial because of limited sampling issues, especially for GOME/ERS-2, and also because of the limited dynamical range of the ozone columns at the reference Northern midlatitudes. However, we found that a simple empirical parameterization applied to the correction factors accounts for most of this dependence. In practice, the differential structures of the tabulated correction factor C_t are weighted by the ratio of the current ozone column V_p and the reference ozone column V_t corresponding to C_t. The tabulated correction factor C_t results from the mean of many individual comparisons, so that V_t is the mean of the corresponding reference ground-based ozone columns. Although V_p is not known, an a priori climatological value can be used as a first approximation. For consistency, this parameterization has been applied to correction factors for all sensors, but it is only significant for SCIAMACHY. This issue will be revisited in the future, as part of our ongoing investigation of other possible choices for reference ozone data sets. In addition, if a separation of the additive and multiplicative components of the differential correction factors is possible, then this would allow us to avoid the ozone column dependence in the LUTs. Figure 7 shows a first example of the improved consistency between the total ozone columns from the individual sensors at the reference stations when the soft-calibration scheme is applied to the level-1 data. Other examples on a global scale will be shown in section 3.

2.4. Error Budget

In this section, we provide estimates for component errors contributing to the total ozone uncertainty from our retrieval algorithm; we distinguish random and systematic contributions. The section concludes with an estimate of the total error itself.

2.4.1. Individual Error Sources

The random error associated with instrument signal-to-noise can be derived easily by the propagation (through the inversion algorithm) of radiance and irradiance statistical errors provided in the level-1 products. For the GOME, GOME-2, and SCIAMACHY instruments, this error is generally less than 0.5% at moderate SZAs and may reach 2% at high SZAs ($>80°$).

A significant source of error in the total ozone retrievals arises from the a priori ozone profile shape. This error is referred to as the *smoothing error*. According to *Rodgers* [2001], this error S_p may be estimated as $S_p = A^T S_a A$ where S_a is the covariance matrix associated with the a priori profile climatology, and A is the averaging kernel, which is an indicator of the sensitivity of the retrieval to the true state. Although the ozone column is retrieved as a single element of the state vector, profile weighting functions K can be computed a posteriori at all wavelengths in the fitting interval, and their weighted sum leads to a profile averaging kernel A [*Van*

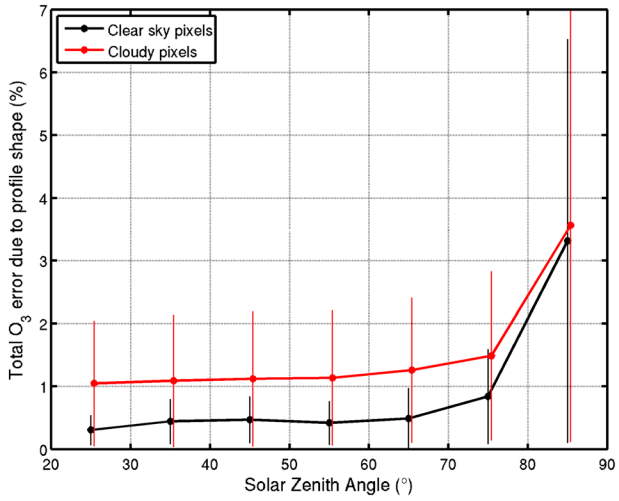

Figure 12. Mean total ozone error due to a priori O_3 profile shape, as a function of the SZA for clear-sky and cloudy pixels. These mean errors have been computed for all climatological profiles; total columns range from 125 to 575 DU. Error bars represent the standard deviation of the errors.

Roozendael et al., 2012; *Spurr et al.*, 2013]. Since we use a profile climatology classified by total ozone columns, the matrix S_a should then represent the covariance of those ozone profiles having an integrated column which matches the retrieved column for a specific latitude band and season. This information could be derived from analysis of the database used to construct the TOMSv8 climatology. This analysis is beyond the scope of the present work; instead, we have used a different total ozone classified climatology as a proxy to construct S_a, namely the dynamical ozone climatology developed at IUP/Bremen [*Lamsal et al.*, 2004]. The total ozone error can then be estimated for different SZAs, taking into account typical averaging kernels for clear and cloudy scenarios. As illustrated in Figure 12, the mean total ozone error due to the profile shape is less than 0.5% for clear-sky pixels at low SZAs, but rises rapidly for higher SZAs. For cloudy pixels, the mean error is generally larger, especially at low SZA. The error bars represent the standard deviation of the errors computed for all individual profiles provided in the climatology for the different latitude bands, months, and total ozone columns.

In GODFIT, both absorption by trace gases other than ozone and the impact of aerosols are neglected in the forward model. Here, we estimate the resulting total ozone errors using closed-loop tests. Synthetic radiances are generated using the GODFIT forward model based on optical inputs that include these sources of error (e.g., NO_2 or aerosols). Then, total ozone retrieval is performed using these synthetic spectra and the retrieval settings baseline (i.e., neglecting other trace gases or aerosols in the forward model). The difference with respect to the "true" state gives the error estimate.

To simulate the impact of stratospheric NO_2, a typical stratospheric profile [*Levelt et al.*, 2009] as depicted in Figure 13 has been used to generate synthetic radiances. Total ozone columns retrieved from the resulting synthetic spectra show errors of less than 0.5% for all SZAs and all surface albedos. When considering a profile with a large amount of NO_2 in the lowermost layer (e.g., representative of a heavily polluted scenario), total ozone errors increase slightly but are still less than 0.5% for low surface albedo (0.05). The errors are slightly

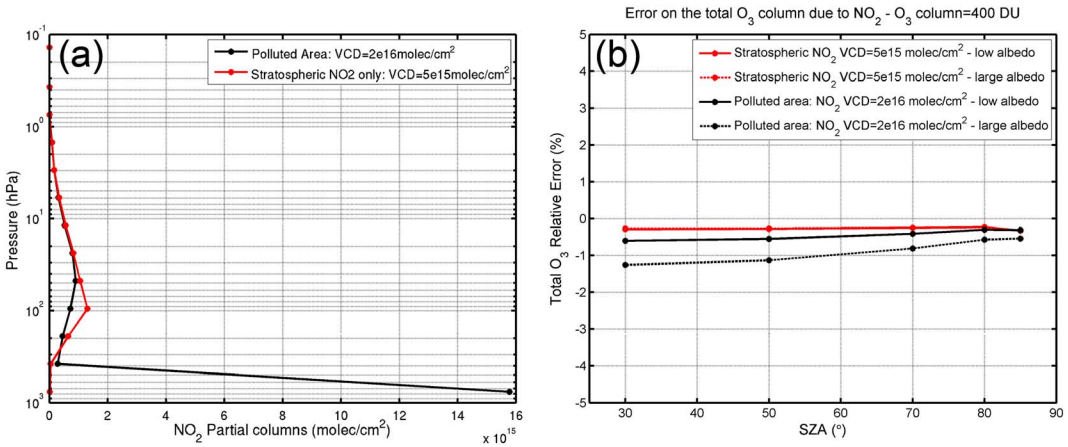

Figure 13. (a) NO_2 vertical profiles used for generating synthetic radiances. (b) Total ozone error (%) due to neglect of NO_2 in the retrieval scheme, as a function of SZA. For the two profiles shown in panel (a), ozone errors are plotted for low and high surface albedos (0.05 and 0.8) and for a total ozone column of 400 DU.

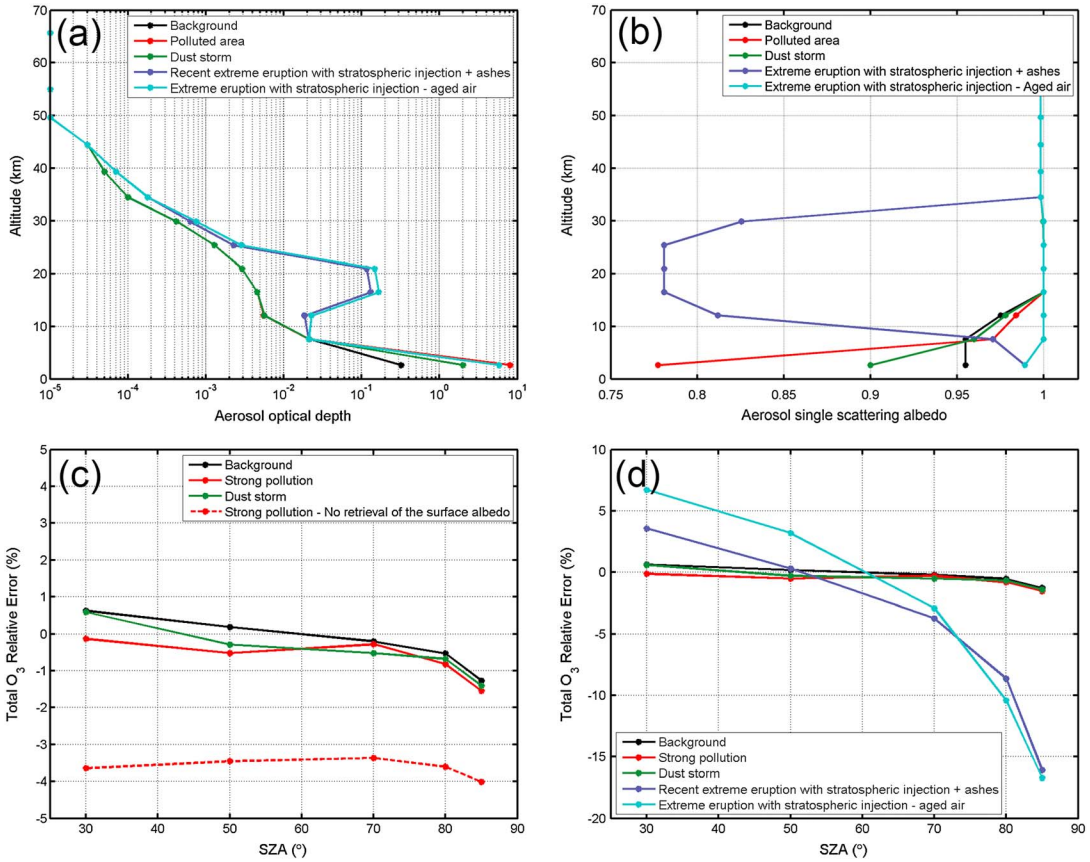

Figure 14. (a) Aerosol optical depth and (b) aerosol single scattering profiles used for generating synthetic radiances for a variety of scenarios (see inset and text for more details). (c) Total ozone error (%) due to neglect of aerosols in the retrieval scheme, plotted as a function of SZA for the background, polluted, and dust storm scenarios. The red dashed line shows the much larger errors obtained when a fixed (nonfitted) albedo is used. (d) Same as Figure 14c but for strong volcanic eruption scenarios.

larger than 1% when the surface albedo is high (0.8), but the likelihood of such a high NO_2 concentration above a bright surface is very small. Similar sensitivity tests have been carried out for BrO and SO_2. The errors due to their neglect are generally negligible, except for a major volcanic eruption scenario with SO_2 column amounts exceeding 50 DU. In this case, total ozone errors may reach a few percent.

The same closed-loop approach has been adopted to estimate the ozone error due to neglect of aerosols in the forward model. A number of scenarios were considered, including a background aerosol case, a heavily polluted scenario with a large amount of absorbing aerosol in the lowermost layer, a dust storm scenario with a large amount of scattering aerosol in the lowermost layer, and finally, two scenarios representing major volcanic eruptions with stratospheric injections of absorbing or scattering aerosols. Optical property profiles for these scenarios are plotted in Figures 14a–14b [*Levelt et al.*, 2009; *Berk et al.*, 2006]. The associated total ozone errors, plotted as a function of SZA in Figure 14c, are generally within 1%. This small impact is mainly due to the simultaneous fit of the effective surface albedo. As seen in Figure 14c for the pollution scenario, total ozone errors are much larger (up to 4%) if the surface albedo is fixed to a climatological value. This nicely illustrates the added value of the internal closure mode of GODFIT, which implicitly accounts for tropospheric absorbing and scattering aerosols and avoids reliance on the ingestion of highly uncertain external aerosol optical property information. For a scenario with a strong injection of stratospheric aerosols due to a major volcanic eruption such as Pinatubo, the total errors may reach 10% (Figure 14d).

Uncertainties associated with the cloud fraction and cloud top height values provided by FRESCOv6 are 0.05 and 1 km, respectively [*Wang et al.*, 2008]. Sensitivity tests have been performed to estimate the impact of these uncertainties on total ozone retrievals. Essentially, we compare the ozone columns retrieved using modified cloud parameters to those retrieved with the original parameter settings. We assume here that these cloud product uncertainties are uncorrelated, and that the impact of each error source can be assessed

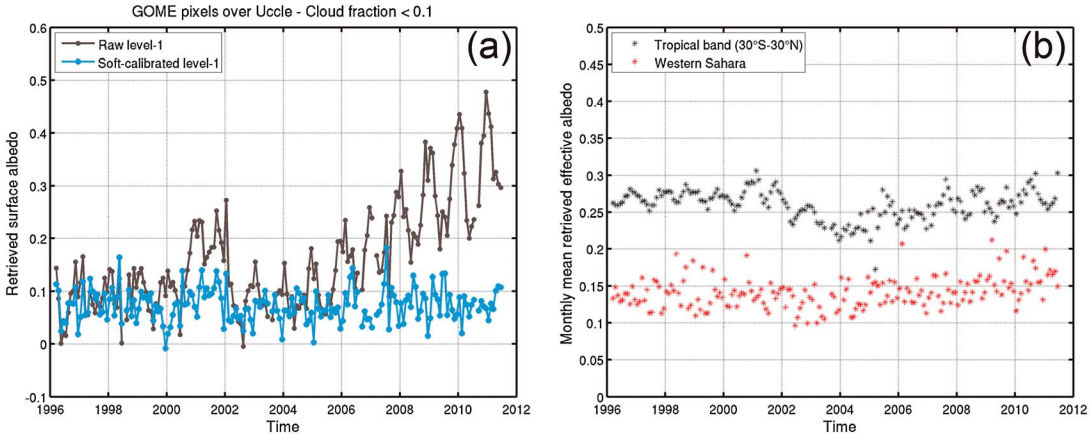

Figure 15. (a) Time series of retrieved effective surface albedo for clear-sky GOME pixels over Uccle (Belgium). The black line shows the values derived from uncorrected level-1 GOME data, while the blue line is based on soft-calibrated GOME data. (b) Time series of retrieved effective surface albedo for all GOME pixels in the Tropics (black dots) and the Western Sahara (red dots).

separately. Cloud fraction uncertainty generally leads to small total ozone error ($<$ 0.5%), while the cloud top height uncertainty may give rise to total ozone errors of up to 1.5%. Under specific conditions (e.g., pixels fully covered by very high clouds), these errors may be significantly larger and are difficult to assess. This issue will be further addressed in the sequel validation paper.

Another significant source of total ozone systematic error is due to uncertainties in the reference ozone cross sections as measured in the laboratory. As noted above, the GODFIT baseline uses the ozone cross sections provided by *Daumont et al.* [1992], *Malicet et al.* [1995], *Brion et al.* [1998]. Recently, new cross sections have been released by the University of Bremen [*Gorshelev et al*., 2013; *Serdyuchenko et al*., 2013]. Although this data set is currently under assessment, preliminary tests show that a switch to this data set would lead to an increase in the ozone columns by 1 to 2.5%, depending on the effective temperature. This level of bias provides a good estimate of intrinsic error in the cross-section data.

The soft-calibration scheme developed in this study is designed to correct for most systematic level-1 errors. However, there are limitations associated with the scheme itself, and this contribution to the total error is relatively difficult to assess. We consider first the absolute soft-calibration correction. A proxy for the total ozone error due to uncertainty in the absolute soft-calibration can be inferred from the time stability of the retrieved effective surface albedo. Figure 15 shows some examples of these time series. Panel (a) compares the albedos retrieved for clear-sky pixels over Uccle (Belgium) from GOME, with and without soft calibration. The added value of the soft calibration correction is obvious: the retrieved albedo is stable over time (within ±0.05) after the correction is applied. Panel (b) shows similar time series based on all GOME pixels in a tropical latitude band. Again, retrieved values are very stable over time. The small discontinuity around 2003 is due to the loss of the GOME global coverage. Focusing on the Western Sahara region (where the coverage is stable over the full mission lifetime), the stability of the retrieved albedo is excellent (±0.05). Also, additional sensitivity tests have been carried out to assess a potential error due to the soft-calibration procedure for a scenario in which the seasonal cycle presented in section 2.3.1.1 would originate entirely from forward model limitations instead of instrumental issues. From these results, we estimate the total ozone error associated with the absolute soft-calibration procedure to be less than 1%.

GODFIT ozone retrieval errors associated with the differential soft-calibration process are strongly linked to errors intrinsic to the eight reference Brewer measurements (section 2.3.1.2). As a proxy for this contribution, we take the standard deviation of the monthly mean differences between the individual reference Brewer and the satellite ozone column measurements. This standard deviation does not vary much over time, and its mean value is close to 1%.

Combining these two contributions leads to a total ozone error from soft calibration of less than 1.5%.

2.4.2. Total Error Budget

Based on the analysis presented in the previous section, Table 5 summarizes the error budget for the column ozone retrieval algorithm. A few error sources (solar I_0 effect, Ring effect, spectral stability) have not been discussed here — the resulting error values are very similar to those already presented in *Van Roozendael*

Table 5. Total Error Budget for Column Ozone Retrieval[a]

Error Source	Percent Error SZA < 80°	Percent Error SZA > 80°
Random Errors		
Instrument signal-to-noise	< 0.5	< 2
Cloud fraction	< 0.5	< 0.5
Cloud top height	< 1.5	< 1.5
Systematic Errors		
Soft calibration: Absolute recalibration + structures removal	< 1.5	< 1.5
O_3 absorption cross sections and its atmospheric temperature	< 2.5	< 2.5
Interferences with other species (except in case of volcanic eruption)	< 1.5	< 1
Aerosols (except in case of volcanic eruption)	< 1	< 1.5
Instrument spectral stability (wavelength registration)	< 0.5	< 0.5
Solar I_0-effect	< 0.2	< 0.2
Ring effect (Rotational Raman Scattering)	< 0.1	< 0.5
O_3 profile shape	< 1	< 4
Total Errors		
Total random error (including cloud fields)	< 1.7	< 2.6
Total systematic error	< 3.6	< 5.3

[a]Random and systematic contributions are distinguished. The errors due to the cloud parameters are random or systematic depending on the time scale but have been considered as random in the total budget.

et al. [2006]. Furthermore, these contributions to the total ozone error are small. We have separated errors for low/moderate SZA scenarios from those for high SZA (>80°). Also, we distinguish random and systematic sources. The errors from cloud parameter uncertainty are either random or systematic, depending on the temporal and/or spatial scales of interest (cloud contamination is extremely variable). In drawing up the total budget, we have considered cloud errors as "pseudo-random." Total errors are computed assuming all contributions are mutually uncorrelated. The total random errors are estimated to be 1.7 and 2.6% for the low/moderate and high SZA regimes, respectively. The corresponding total systematic errors are about 3.6 and 5.3%. Note that without the soft-calibration procedure, these systematic errors could be much larger (6–7%).

3. Initial Results

3.1. Intersensor Comparison

First, we focus on the mutual consistency between individual level-2 data sets generated from GOME/ERS-2, SCIAMACHY/Envisat, and GOME-2/MetOp-A. Figure 16 illustrates total ozone relative differences between SCIAMACHY and GOME on the one hand, and between GOME-2 and GOME on the other. Results are presented as a function of the latitude and time. These comparisons are shown for the current ESA and EUMETSAT operational products, and for the reprocessed CCI GODFITv3 data sets. The current ESA operational products for GOME and SCIAMACHY are GDP v5 and SGP v5.02, respectively [*Van Roozendael et al*., 2012; *Lerot et al*., 2009] and the operational GOME-2 total ozone product provided by EUMETSAT O3M-SAF is GDP v4.6 [*Loyola et al*., 2011]. In constructing these comparisons, we use only those daily measurements for regions sampled by any pair of instruments. This is particularly important in the light of the GOME global coverage loss in June 2003, and also for the sparser daily coverage of SCIAMACHY (global coverage in six days only due to its alternating nadir and limb measurement modes).

The SCIAMACHY and GOME operational products generally agree quite well (within 2%). Note that an empirical scale factor has been applied to the ozone cross sections as used in the SCIAMACHY operational processor, in order to maintain a good agreement with GOME in early 2003 soon after the start of the Envisat mission [*Lerot et al*., 2009]. Without this scale factor, the SCIAMACHY-GOME differences would be much larger and consistent with those shown in Figure 7. In general, relative ozone differences tend to increase over time at all latitudes. The differences between GOME-2 GDP v4.6 and GOME GDP v5 ozone are larger, especially in Tropics where GOME-2 columns are about 2% lower than those from GOME. In addition, these differences further increase at all latitudes after the GOME-2 throughput tests carried out in late 2009. Also, significant differences are visible in ozone hole scenarios. Considering the GODFITv3 data sets (lower Panels of Figure 16), it is clear that the total ozone differences from the individual sensors are much smaller and more homogeneous over time and

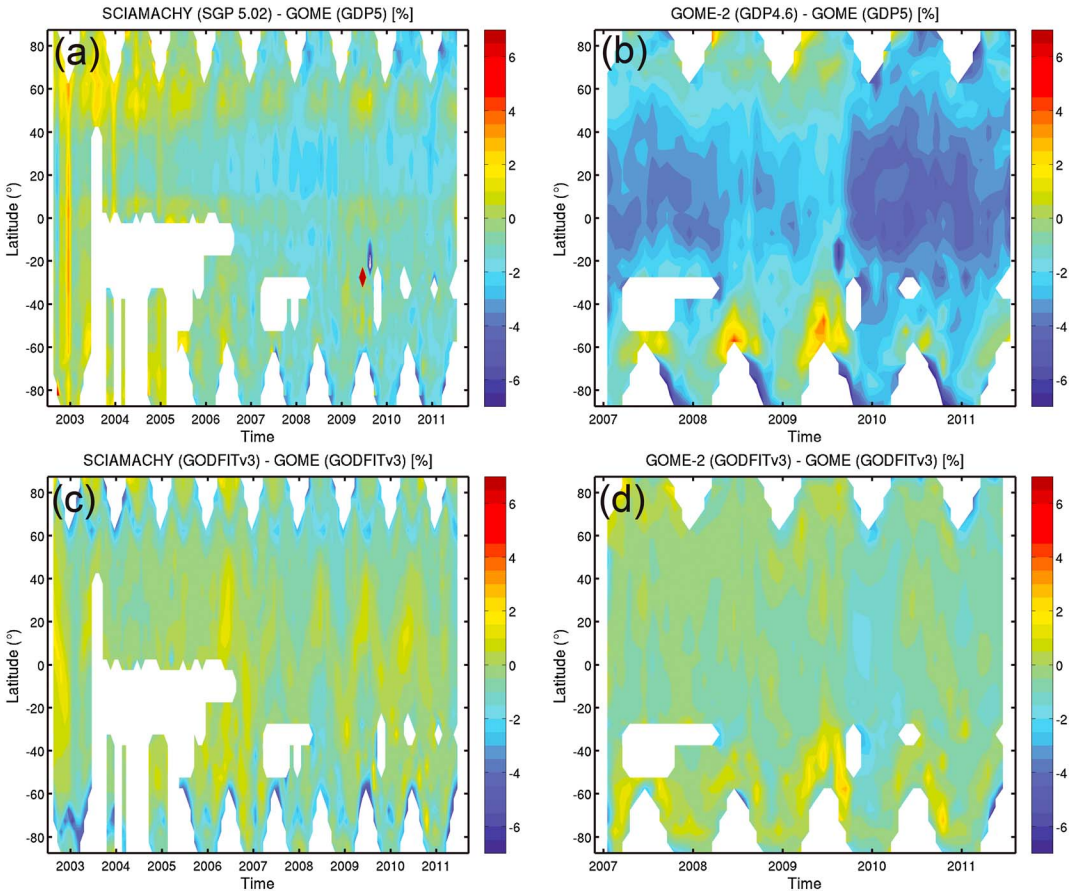

Figure 16. Illustration of the European intersensor consistency. Panels (a) and (b) show the latitude/time cross section of the relative differences between the current ESA GOME (GDP v5) and SCIAMACHY (SGP v5.02), and EUMETSAT O3M-SAF GOME-2 (GDP v4.6) operational total O_3 products. Panels (c) and (d) show similar plots, but now using the ESA CCI GODFITv3 products. With significant reductions in bias, long-term drift and seasonal differences, the improvement of the intersensor consistency is clear.

latitude. Although some slightly larger differences remain at the terminator (extreme SZAs), this overall improved consistency nicely shows the added value of deploying the level-1 soft-calibration scheme, in addition to the use of common retrieval settings for the three sensors. Also, it is worth noting that the GOME spectral feature LUT has no time dependence, in contrast with the two other sensors (see section 2.3.2). Since no significant drift is apparent in the SCIAMACHY vs. GOME and GOME-2 vs. GOME differences, this indicates that the reference Brewer data sets used for the soft-calibration have been appropriately selected.

Figure 17 compares the three GODFITv3 data sets with the recently released merged Solar Backscatter Ultraviolet Radiometer (SBUV) v8.6 data record [*Bhartia et al*., 2013; *McPeters et al*., 2013] in different latitude bands. This comparison is based on monthly zonal means for each product. The GODFIT data sets agree excellently with the SBUV record in tropical and midlatitude regions, where the differences are generally within 1%. Again, the outstanding consistency between the different European sensors is clearly visible. In Polar Regions, in spite of good overall agreement, departures from the SBUV record can be larger (up to 5%). This is not surprising, since geophysical conditions in these regions are most extreme (very large SZAs, strong ozone spatial gradients, highly variable surface albedo, etc.), resulting in enhanced sensitivity to algorithmic differences. In addition, the coverage and the solar local time sampling of the SBUV instruments differ from those of the GOME, SCIAMACHY, and GOME-2 sensors, which may significantly impact the zonal mean differences in these high latitude regions with strong and variable ozone spatial gradients.

3.2. Summary of Validation Results

In order to assess the quality of the new GODFITv3 data sets, total ozone column measurements from monitoring networks contributing to WMO's Global Atmosphere Watch, routinely archived at the World Ozone and Ultraviolet

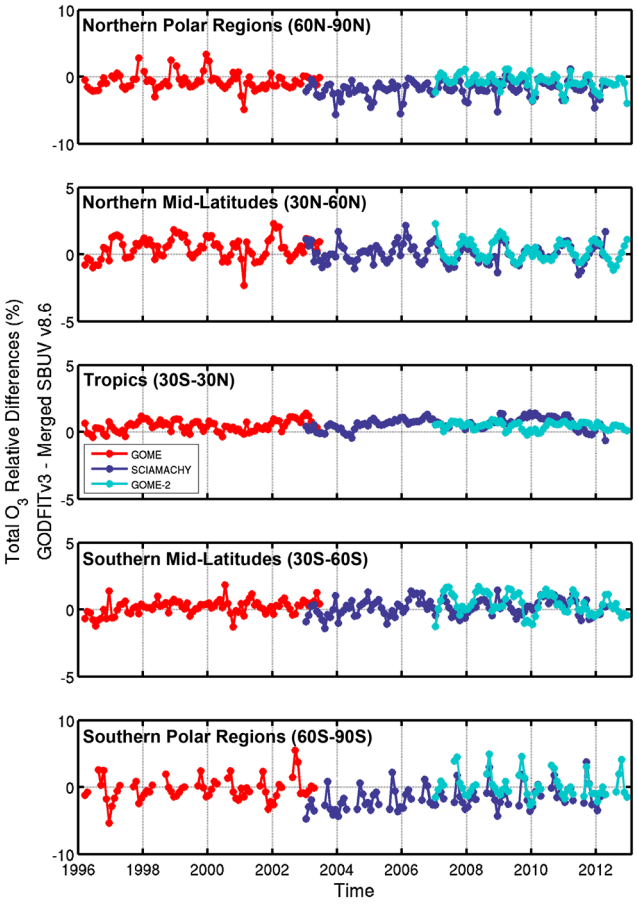

Figure 17. Relative total ozone differences between the monthly zonal mean of GODFITv3 GOME, SCIAMACHY, and GOME-2 data and that from the merged SBUV v8.6 product, plotted as a function of time for five different latitude bands.

Data Centre (WOUDC) (http://www.woudc.org) and the Data Host Facility of the Network for the Detection of Atmospheric Composition Change (NDACC, http://ndacc.org), were used as ground reference for comprehensive comparisons. The WOUDC and NDACC archives contain total ozone column data mainly from Dobson and Brewer UV spectrophotometers and from UV–Visible DOAS spectrometers. A well-maintained and calibrated Dobson spectrophotometer measures the ozone column with an estimated total uncertainty of 1% for direct Sun observations and 2–3% for zenith sky observations at sun elevations higher than 15°. The selection of WOUDC and NDACC stations for total ozone validation has already been discussed in a number of papers, including the validation of 10 years of GOME observations [*Balis et al.*, 2007b], validation of OMI-TOMS and OMI-DOAS data sets [*Balis et al.*, 2007a], of the GOME-2 GDP v4.6 product [*Loyola et al.*, 2011; *Koukouli et al.*, 2012], and of the SBUV measurements [*Labow et al.*, 2013].

In Figure 18, the current operational data sets for GOME, SCIAMACHY, and GOME-2 (panels (a) and (b)) and the GODFITv3 data sets (panels (c) and (d)) are compared with the Brewer and Dobson measurements in the Northern Hemisphere. With respect to the Brewer network, the agreement between the three instruments has improved significantly with GODFITv3, with a far smoother GOME record oscillating around 0.5%, a more stable SCIAMACHY time series without any discontinuity, and an improved GOME-2 data set now very consistent with those from GOME and SCIAMACHY. A similar picture emerges from the Dobson comparisons, although a yearly cycle and a +1% bias is visible. The seasonality is mostly caused by the temperature dependence of the Dobson measurements themselves [*Scarnato et al.*, 2009]. Nevertheless, these Dobson comparisons also illustrate the higher level of homogeneity and of mutual consistency in the GODFITv3 total ozone data sets. In the Southern Hemisphere [not shown here], a significant improvement in the intersensor consistency is also observed, along with a considerable reduction of the scatter for the SCIAMACHY and GOME-2 data sets.

In the sequel validation paper, more detailed comparisons will be shown, and dependencies with respect to other geophysical parameters such as SZA and temperature will be investigated. In addition, validation results for these GODFITv3 data sets will be compared to those obtained with respect to other well-documented total ozone records such as the SBUV time series.

4. Summary and Outlook

As part of the ESA ozone CCI project, total ozone data sets have been recently reprocessed with the retrieval algorithm GODFIT (version 3), for the entire time series of the GOME/ERS-2, SCIAMACHY/Envisat, and GOME-2/MetOp-A observations. The direct-fitting GODFIT algorithm leads to high quality retrievals in all conditions, including high solar zenith angles and large optical depths. Since the deployment of the GODFIT version used in the

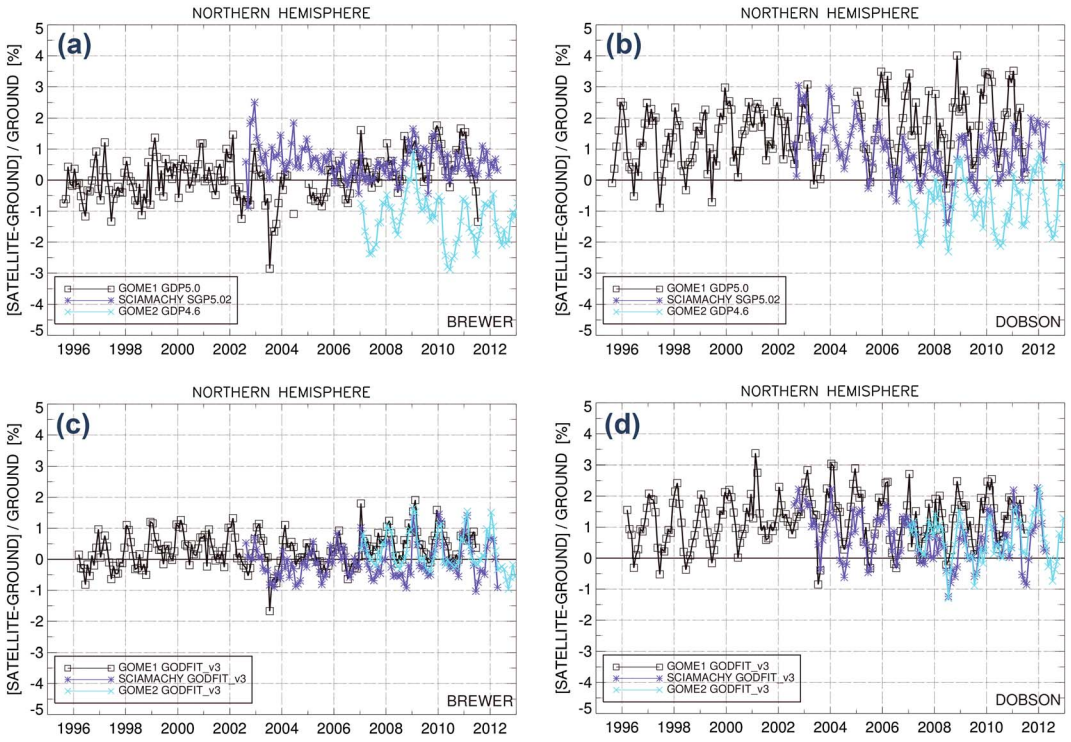

Figure 18. Monthly mean relative total ozone differences between satellite and ground-based data (Brewer network: panels (a) and (c); Dobson network: panels (b) and (d)). Results are averaged over the Northern Hemisphere and plotted as a function of time. Compared to the current operational GOME, SCIAMACHY and GOME2 products, namely, GDP v5.0, SGP v5.02, and GDP v4.6, respectively (panels (a) and (b)), the behavior of the new GODFITv3 data sets (panels (c) and (d)) improves significantly in homogeneity, bias, long-term stability, shorter-term noise, and mutual consistency.

GOME operational ground segment (GDP v5) [*Van Roozendael et al.*, 2012], a number of new developments in GODFIT have made the algorithm even more robust. First, the a priori tropospheric ozone content has been improved by combining the total ozone climatology TOMSv8 with a recent tropospheric ozone column climatology based on OMI and MLS measurements [*Ziemke et al.*, 2011]. This is particularly important in Tropical Regions where contamination with convective clouds may significantly impact the retrieval if inappropriate a priori information is used. Second, the Ring correction has been upgraded using an improved semi-empirical formulation, and radiances simulated with the scalar radiative transfer model LIDORT are now corrected for atmospheric polarization. These new features bring the algorithm closer to the physics, especially when an effective surface albedo is retrieved simultaneously with the ozone column. Third, the computational performance of the retrievals has been significantly enhanced through the implementation of fast PCA-based radiative transfer tools which take advantage of data redundancy in optical properties pertinent to the ozone fitting window [*Spurr et al.*, 2013]. This has greatly facilitated the application of GODFIT to the most recent sensors.

Although common retrieval settings are used for all three sensors, significant differences may appear when individual data sets are compared; this is largely due to remaining calibration issues in the level-1 data. To improve intersensor consistency, a soft-calibration scheme for measured reflectances has been developed. This procedure relies on a statistical comparison of the level-1 sun-normalized radiances with spectra simulated using Brewer ozone measurements at a few reference sites. The identification and correction of any artificial offsets or spectral structures in the measured reflectances greatly improve the agreement between individual level-2 total ozone data sets. This improved consistency has been demonstrated through intersensor comparisons, including with the merged SBUV v8.6 data record. An initial summary of the ground-based validation results also illustrates the high quality of the GODFIT V3 data sets; a detailed examination of the validation results will be published in the sequel paper.

Together, these European satellite level-2 data sets span the time period 1996–2012 and their high quality makes them suitable for climate research and monitoring applications. The data sets can be downloaded from the ozone CCI website (http://www.esa-ozone-cci.org/). A homogeneous level-3 record based on the

merging of these individual level-2 data sets has also been constructed, and this is the subject of the third paper in the series.

In the future, the ESA CCI total ozone record will be extended by applying our GODFIT retrieval algorithm to GOME-2 on MetOp-B (launched in September 2012), to OMI on AURA (2004 onward) and to future sensors such as GOME-2 on MetOp-C and TROPOMI on board the Sentinel-5 Precursor platform. The latter instrument is planned for launch in 2015 and will provide daily global coverage with an unprecedented high spatial resolution of 7×7 km^2.

During the next phase of the ESA CCI project, further algorithmic developments are planned. In particular, an alternative to the current cloud correction will be investigated. Instead of assuming the clouds as Lambertian reflectors, a more realistic model will be tested in which clouds are treated as a set of contiguous optically uniform scattering layers. In addition, further improvements to the level-1 soft-calibration scheme are planned. Instead of a subset of Brewer instruments providing the reference ozone for simulating reflectances, we will investigate the possibility to use a combination of several satellite instruments covering the entire period of interest. This would circumvent the limited sampling problem (correction-factor LUTs could have more dimensions, only clear-sky pixels could be selected, etc.), and the satellite total ozone record would remain totally independent from the ground-based network.

Acknowledgments

This work has been performed as part of the Ozone_cci project (a component of the ESA Climate Change Initiative program, ESRIN/Contract 4000101683/10/I-NB), with additional support provided through the Belspo SPP Science Policy "Chercheur Supplémentaire 2011" grant 60.11.45.23 at the Belgian Institute for Space Aeronomy (BIRA-IASB). The authors would like to thank ESA for provision of GOME and SCIAMACHY level-1 and level-2 products through the DLR D-PAF and D-PAC contracts. We thank EUMETSAT for provision of the GOME-2 level-1 data, and O3M-SAF for operational GOME-2 total ozone products. Temperature profiles ingested in the soft-calibration scheme were provided by ECMWF. The SBUV team is gratefully acknowledged for provision of their merged zonal mean total ozone record. The ground-based data used in this work and in the validation were obtained from the World Ozone and UV Data Centre (WOUDC) and the Network for the Detection of Atmospheric Composition Change (NDACC), and are publicly available (see http://woudc.org and http://ndacc.org).

References

Austin, J., et al. (2010), Decline and recovery of total column ozone using a multimodel time series analysis, *J. Geophys. Res.*, *115*, D00M10, doi:10.1029/2010JD013857.

Balis, D., M. Kroon, M. E. Koukouli, E. J. Brinksma, G. Labow, J. P. Veefkind, and R. D. McPeters (2007a), Validation of Ozone Monitoring Instrument total ozone column measurements using Brewer and Dobson spectrophotometer ground-based observations, *J. Geophys. Res.*, *112*, D24S46, doi:10.1029/2007JD008796.

Balis, D., et al. (2007b), Ten years of GOME/ERS2 total ozone data—The new GOME data processor (GDP) version 4: 2. Ground-based validation and comparisons with TOMS V7/V8, *J. Geophys. Res.*, *112*, D07307, doi:10.1029/2005JD006376.

Bekki, S., et al. (2011), Future ozone and its impact on surface UV, Chapter 3 in Scientific Assessment of Ozone Depletion: 2010, in *Global Ozone Research and Monitoring Project – Report No. 52*, pp. 516, World Meteorological Organization, Geneva, Switzerland.

Bekki, S., A. Rap, V. Poulain, S. Dhomse, M. Marchand, F. Lefevre, P. M. Forster, S. Szopa, and M. P. Chipperfield (2013), Climate impact of stratospheric ozone recovery, *Geophys. Res. Lett.*, *40*, 2796–2800, doi:10.1002/grl.50358.

Berk, A., et al. (2006), MODTRAN5: 2006 Update, Proc. SPIE, Vol. 6233, 62331F.

Bhartia, P. K., and C. W. Wellemeyer (2002), TOMS-V8 Total O_3Algorithm, OMI Algorithm Theoretical Basis Document, available at http://www.knmi.nl/omi/documents/data/OMI_ATBD_Volume_2_V2.pdf.

Bhartia, P. K., R. D. McPeters, L. E. Flynn, S. Taylor, N. A. Kramrova, S. Frith, B. Fisher, and M. DeLand (2013), Solar Backscatter UV (SBUV) total ozone and profile algorithm, *Atmos. Meas. Tech.*, *6*, 2533–2548, doi:10.5194/amt-6-2533-2013.

Bovensmann, H., J. Burrows, M. Buchwitz, J. Frerick, S. Noel, V. Rozanov, K. Chance, and A. Goede (1999), SCIAMACHY: Mission Objectives and Measurement Modes, *J. Atmos. Sci.*, *56*, 127–150.

Bramstedt, K. (2008), Calculation of SCIAMACHY M-Factors, Technical Note, IFE-SCIA-TN-2007-01-CalcMFactor, Issue: 1, available at http://www.iup.uni-bremen.de/sciamachy/mfactors/.

Brion, J., A. Chakir, J. Charbonnier, D. Daumont, C. Parisse, and J. Malicet (1998), Absorption spectra measurements for the ozone molecule in the 350–830 nm region, *J. Atmos. Chem.*, *30*, 291–299, doi:10.1023/A:1006036924364.

Burrows, J., et al. (1999), The Global Ozone Monitoring Experiment (GOME): Mission concept and first scientific results, *J. Atmos. Sci.*, *56*, 151–175.

Cai, Z., Y. Liu, X. Liu, K. Chance, C. R. Nowlan, R. Lang, R. Munro, and R. Suleiman (2012), Characterization and correction of Global Ozone Monitoring Experiment 2 ultraviolet measurements and application to ozone profile retrievals, *J. Geophys. Res.*, *117*, D07305, doi:10.1029/2011JD017096.

Chance, K., and R. L. Kurucz (2010), An improved high-resolution solar reference spectrum for Earth's atmosphere measurements in the ultraviolet, visible, and near infrared, *J. Quant. Spectrosc. Radiat. Transfer*, *111*, 1289–1295, doi:10.1016/j.jqsrt.2010.01.036.

Chance, K., and R. Spurr (1997), Ring effect studies: Rayleigh scattering including molecular parameters for rotational Raman scattering, and the Fraunhofer spectrum, *Appl. Opt.*, *36*, 5224–5230, doi:10.1364/AO.36.005224.

Coldewey-Egbers, M., M. Weber, L. N. Lamsal, R. de Beek, M. Buchwitz, and J. P. Burrows (2005), Total ozone retrieval from GOME UV spectral data using the weighting function DOAS approach, *Atmos. Chem. Phys.*, *5*, 1015–1025, doi:10.5194/acp-5-1015-2005.

Coldewey-Egbers, M., S. Slijkhuis, B. Aberle, and D. Loyola (2008), Long-term analysis of GOME in-flight calibration parameters and instrument degradation, *Appl. Opt.*, *47*(28), 4749–4761, doi:10.1364/AO.47.004749.

Daumont, D., J. Brion, J. Charbonnier, and J. Malicet (1992), Ozone UV spectroscopy. I. Absorption cross-sections at room temperature, *J. Atmos. Chem.*, *15*, 145–155, doi:10.1007/BF00053756.

Dee, D. P., et al. (2011), The ERA-Interim reanalysis: configuration and performance of the data assimilation system, *Q. J. R. Meteorol. Soc.*, *137*, 553–597, doi:10.1002/qj.828.

Dentener, F., et al. (2006), The global atmospheric environment for the next generation, *Environ. Sci. Technol.*, *40*(11), 3586–3594.

Eyring, V., et al. (2007), Multimodel projections of stratospheric ozone in the 21st century, *J. Geophys. Res.*, *112*, D16303, doi:10.1029/2006JD008332.

Fleming, E. L., C. H. Jackman, R. S. Stolarski, and A. R. Douglass (2011), A model study of the impact of source gas changes on the stratosphere for 1850–2100, *Atmos. Chem. Phys.*, *11*, 8515–8541, doi:10.5194/acp-11-8515-2011.

GCOS (2011), Systematic Observation Requirements for Satellite-based products for Climate - 2011 Update, GCOS 154, available at http://www.wmo.int/pages/prog/gcos/Publications/gcos-154.pdf.

Gorshelev, V., A. Serdyuchenko, M. Weber, W. Chehade, and J. P. Burrows (2013), High spectral resolution ozone absorption cross-sections - Part 1: Measurements, data analysis and comparison with previous measurements around 293K, *Atmos. Meas. Tech. Discuss.*, *6*, 6567–6611, doi:10.5194/amtd-6-6567-2013.

Grainger, J. F., and J. Ring (1962), Anomalous Fraunhofer line profiles, *Nature*, *193*, 762, doi:10.1038/193762a0.

Kleipool, Q. L., M. R. Dobber, J. F. de Haan, and P. F. Levelt (2008), Earth surface reflectance climatology from 3 years of OMI data, *J. Geophys. Res.*, *113*, D18308, doi:10.1029/2008JD010290.

Koukouli, M., D. Balis, D. Loyola, P. Valks, W. Zimmer, N. Hao, J.-C. Lambert, M. Van Roozendael, C. Lerot, and R. Spurr (2012), Geophysical validation and long-term consistency between GOME-2/MetOp-A total ozone column and measurements from the sensors GOME/ERS-2, SCIAMACHY/ENVISAT and OMI/Aura, *Atmos. Meas. Tech.*, *5*, 2169–2181.

Krijger, J. M., I. Aben, and J. Landgraf (2005), CHEOPS-GOME: WP2.1: Study of instrument degradation, ESA SRON-EOS:RP/05-018 Tech. rep.

Labow, G. J., R. D. McPeters, P. K. Bhartia, and N. Kramarova (2013), A comparison of 40 years of SBUV measurements of column ozone with data from the Dobson/Brewer network, *J. Geophys. Res. Atmos.*, *118*, 7370–7378, doi:10.1002/jgrd.50503.

Lambert, J.-C., M. Koukouli, D. Balis, J. Granville, C. Lerot, and M. Van Roozendael (2012), GDP 5.0 - Upgrade of the GOME Data Processor for Improved Total Ozone Column: Validation Report, TN-IASB-GOME-GDP5-VR, available at https://earth.esa.int/web/guest/document-library/browse-document-library/-/article/gome-gdp-5-validation-report.

Lamsal, L. N., M. Weber, S. Tellmann, and J. P. Burrows (2004), Ozone column classified climatology of ozone and temperature profiles based on ozonesonde and satellite data, *J. Geophys. Res.*, *109*, D20304, doi:10.1029/2004JD004680.

Lang, R. (2012), GOME-2 / MetOp-A instrument, PPF and auxiliary-data change history, EUM/OPS-EPS/TEN/08/0716, EUMETSAT, Darmstadt, Germany, available at http://oiswww.eumetsat.org/epsreports/html/history/MetOpAGOME2PPFhist.pdf.

Lerot, C., M. Van Roozendael, J. van Geffen, J. van Gent, C. Fayt, R. Spurr, G. Lichtenberg, and A. von Bargen (2009), Six years of total ozone column measurements from SCIAMACHY nadir observations, *Atmos. Meas. Tech.*, *2*, 87–98, doi:10.5194/amt-2-87-2009.

Lerot, C., M. van Roozendael, J. van Gent, D. Loyola, and R. Spurr (2010), The GODFIT algorithm: A direct fitting approach to improve the accuracy of total ozone measurements from GOME, *Int. J. Remote Sens.*, *31*, 543–550, doi:10.1080/01431160902893576.

Levelt, P. F., J. P. Veefkind, B. J. Kerridge, R. Siddans, G. de Leeuw, J. Remedios, and P. F. Coheur (2009), Chemistry of the Atmosphere Mission concEpts and sentineL Observations Techniques: Final Report, Issue 1, Ed. J. P. Veefkind, available at http://www.knmi.nl/research/climate_observations/future_mission_studies/camelot.php.

Liu, X., K. Chance, and T. P. Kurosu (2007a), Improved ozone profile retrievals from GOME data with degradation correction in reflectance, *Atmos. Chem. Phys.*, *7*, 1575–1583, doi:10.5194/acp-7-1575-2007.

Liu, X., K. Chance, C. Sioris, and T. Kurosu (2007b), Impact of using different ozone cross sections on ozone profile retrievals from Global Ozone Monitoring Experiment (GOME) ultraviolet measurements, *Atmos. Chem. Phys.*, *7*, 3571–3578, doi:10.5194/acp-7-3571-2007.

Loyola, D., W. Thomas, Y. Livschitz, T. Ruppert, P. Albert, and R. Hollmann (2007), Cloud properties derived from GOME/ERS-2 backscatter data for trace gas retrieval, *IEEE Trans. Geosci. Remote Sens.*, *45*(9), 2747–2758, doi:10.1109/TGRS.2007.901043.

Loyola, D., et al. (2011), The GOME-2 total column ozone product: Retrieval algorithm and ground-based validation, *J. Geophys. Res.*, *116*, D07302, doi:10.1029/2010JD014675.

Malicet, J., D. Daumont, J. Charbonnier, C. Parisse, A. Chakir, J. Brion, and U. V. Ozone (1995), Spectroscopy. II. Absorption cross-sections and temperature dependence, *J. Atmos. Chem.*, *21*, 263–273, doi:10.1007/BF00696758.

McPeters, R. D., G. J. Labow, and J. A. Logan (2007), Ozone climatological profiles for satellite retrieval algorithms, *J. Geophys. Res.*, *112*, D05308, doi:10.1029/2005JD006823.

McPeters, R. D., P. K. Bhartia, D. Haffner, G. J. Labow, and L. Flynn (2013), The version 8.6 SBUV ozone data record: An overview, *J. Geophys. Res. Atmos.*, *118*, 8032–8039, doi:10.1002/jgrd.50597.

Mishchenko, M. I., A. A. Lacis, and L. D. Travis (1994), Errors induced by the neglect of polarization in radiance calculations for Rayleigh-scattering atmospheres, *J. Quant. Spectrosc. Radiat. Transfer*, *51*(3), 491–510.

Munro, R., M. Eisinger, C. Anderson, J. Callies, E. Corpaccioli, R. Lang, A. Lefebvre, Y. Livschitz, and A. Perez Albinana (2006), GOME-2 on MetOp: From in-orbit verification to routine operations, in *Proceedings of EUMETSAT Meteorological Satellite Conference*, Helsinki, Finland.

Rodgers, C. (2001), *Inverse Methods for Atmospheres: Theory and Practice*, World Scientific Press, Singapore.

Scarnato, B., J. Staehelin, T. Peter, J. Gröbner, and R. Stübi (2009), Temperature and slant path effects in Dobson and Brewer total ozone measurements, *J. Geophys. Res.*, *114*, D24303, doi:10.1029/2009JD012349.

Serdyuchenko, A., V. Gorshelev, M. Weber, W. Chehade, and J. P. Burrows (2013), High spectral resolution ozone absorption cross-sections - Part 2: Temperature dependence, *Atmos. Meas. Tech. Discuss.*, *6*, 6613–6643, doi:10.5194/amtd-6-6613-2013.

Snel, R. (2000), In-orbit optical path degradation: GOME experience and SCIAMACHY prediction, ERS Envisat Symposium, SP-461, Göteborg, Sweden.

Snel, R., and J. M. Krijger (2009), An improved scanner model for SCIAMACHY, Technical note, SRON, available at ftp://ftp.sron.nl/pub/ralphs/SNEL_mirror_model.pdf.

Spurr, R. (2008), LIDORT and VLIDORT: Linearized pseudo-spherical scalar and vector discrete ordinate radiative transfer models for use in remote sensing retrieval problems, in *Light Scattering Reviews*, vol. 3, pp. 229–275, edited by A. Kokhanovsky, Springer-Praxis, Chichester, U. K.

Spurr, R. J. D., J. de Haan, R. van Oss, and A. Vasilkov (2008), Discrete ordinate theory in a stratified medium with first order rotational Raman Scattering; A general Quasi-Analytic solution, *J. Quant. Spectrosc. Radiat. Transfer*, *109*, 404–425, doi:10.1016/j.jqsrt.2007.08.011.

Spurr R., and V. Natraj (2011), A linearized two-stream radiative transfer code for fast approximation of multiple-scatter fields, *J. Quant. Spectrosc. Radiat. Transfer*, *112*(16), 2630–2637, ISSN 0022–4073, doi:10.1016/j.jqsrt.2011.06.014.

Spurr, R., V. Natraj, C. Lerot, M. Van Roozendael, and D. Loyola (2013), Linearization of the principal component analysis method for radiative transfer acceleration: application to retrieval algorithms and sensitivity studies, *J. Quant. Spectrosc. Radiat. Transfer*, *125*, 1–17, ISSN 0022–4073, doi:10.1016/j.jqsrt.2013.04.002.

Tilstra, L. G., M. de Graaf, I. Aben, and P. Stammes (2012), In-flight degradation correction of SCIAMACHY UV reflectances and Absorbing Aerosol Index, *J. Geophys. Res.*, *117*, D06209, doi:10.1029/2011JD016957.

van der A, R. J., R. F. van Oss, A. J. M. Piters, J. P. F. Fortuin, Y. J. Meijer, and H. M. Kelder (2002), Ozone profile retrieval from recalibrated Global Ozone Monitoring Experiment data, *J. Geophys. Res.*, *107*(D15), 4239, doi:10.1029/2001JD000696.

van der A, R. J., M. A. F. Allaart, and H. J. Eskes (2010), Multi sensor reanalysis of total ozone, *Atmos. Chem. Phys.*, *10*, 11,277–11,294, doi:10.5194/acp-10-11277-2010.

Van Roozendael, M., V. Soebijanta, C. Fayt, and J.-C. Lambert (2002), Investigation of DOAS issues affecting the accuracy of the GDP version 3.0 total ozone product, in *ERS-2 GOME GDP 3.0 Implementation and Delta Validation*, edited by J.-C. Lambert, Rep. ERSE-DTEX-EOAD-TN-

02– 0006, pp. 97–129, Eur. Space Res. Inst., Eur. Space Agency, Frascati, Italy, available at http://earth.esa.int/pub/ESA_DOC/GOME/gdp3/gdp3.pdf.

Van Roozendael, M., et al. (2006), Ten years of GOME/ERS-2 total ozone data: The new GOME Data Processor (GDP) version 4: 1. Algorithm description, *J. Geophys. Res.*, *111*, D14311, doi:10.1029/2005JD006375.

Van Roozendael, M., et al. (2012), Sixteen years of GOME/ERS-2 total ozone data: The new direct-fitting GOME Data Processor (GDP) version 5—Algorithm description, *J. Geophys. Res.*, *117*, D03305, doi:10.1029/2011JD016471.

Wagner, T., S. Beirle, and T. Deutschmann (2009), Three-dimensional simulation of the Ring effect in observations of scattered sun light using Monte Carlo radiative transfer models, *Atmos. Meas. Tech.*, *2*, 113–124, doi:10.5194/amt-2-113-2009.

Wang, P., P. Stammes, R. van der A, G. Pinardi, and M. van Roozendael (2008), FRESCO+: An improved O2 A-band cloud retrieval algorithm for tropospheric trace gas retrievals, *Atmos. Chem. Phys.*, *8*, 6565–6576, doi:10.5194/acp-8-6565-2008.

Wellemeyer, C., S. Taylor, C. Seftor, R. McPeters, and P. Bhartia (1997), A correction for total ozone mapping spectrometer profile shape errors at high latitude, *J. Geophys. Res.*, *102*, 9029–9038, doi:10.1029/96JD03965.

Ziemke, J. R., S. Chandra, A. M. Thompson, and D. P. McNamara (1996), Zonal asymmetries in southern hemisphere column ozone: Implications of biomass burning, *J. Geophys. Res.*, *101*(D9), 14,421–14,427, doi:10.1029/96JD01057.

Ziemke, J. R., S. Chandra, G. J. Labow, P. K. Bhartia, L. Froidevaux, and J. C. Witte (2011), A global climatology of tropospheric and stratospheric ozone derived from Aura OMI and MLS measurements, *Atmos. Chem. Phys.*, *11*, 9237–9251.